IOP PUBLISHING JOURNAL OF PHYSICS D: APPLIED PHYSICS

J. Phys. D: Appl. Phys. **42** (2009) 143001 (20pp) doi:10.1088/0022-3727/42/14/143001

TOPICAL REVIEW

CCD-based thermoreflectance microscopy: principles and applications

M Farzaneh[1,8], K Maize[2], D Lüerßen[3,4,9], J A Summers[3], P M Mayer[4,10], P E Raad[5,6], K P Pipe[7], A Shakouri[2], R J Ram[4] and Janice A Hudgings[3]

[1] Department of Physics, Kenyon College, Gambier, OH 43022, USA
[2] Department of Electrical Engineering, University of California Santa Cruz, Santa Cruz, CA 95064, USA
[3] Department of Physics, Mount Holyoke College, South Hadley, MA 01075, USA
[4] Research Laboratory of Electronics, Massachusetts Institute of Technology, Cambridge, MA 02139, USA
[5] Department of Mechanical Engineering, Southern Methodist University, Dallas, TX 75275, USA
[6] TMX Scientific, Inc., Dallas, TX 75024, USA
[7] Department of Mechanical Engineering, University of Michigan, Ann Arbor, MI 48109, USA

E-mail: farzanehm@kenyon.edu

Received 23 February 2009, in final form 5 May 2009
Published 29 June 2009
Online at stacks.iop.org/JPhysD/42/143001

Abstract
CCD-based thermoreflectance microscopy has emerged as a high resolution, non-contact imaging technique for thermal profiling and performance and reliability analysis of numerous electronic and optoelectronic devices at the micro-scale. This thermography technique, which is based on measuring the relative change in reflectivity of the device surface as a function of change in temperature, provides high-resolution thermal images that are useful for hot spot detection and failure analysis, mapping of temperature distribution, measurement of thermal transient, optical characterization of photonic devices and measurement of thermal conductivity in thin films. In this paper we review the basic physical principle behind thermoreflectance as a thermography tool, discuss the experimental setup, resolutions achieved, signal processing procedures and calibration techniques, and review the current applications of CCD-based thermoreflectance microscopy in various devices.

(Some figures in this article are in colour only in the electronic version)

1. Introduction

One of the biggest challenges in operation of electronic and optoelectronic devices and integrated circuits (ICs) is the generation of excess heat and increase in temperature under operating conditions. This can cause the loss of reliability, affect the performance or result in catastrophic failure of the device [1]. Additionally, by miniaturization and monolithic integration of sub-micrometre devices on a chip, access to individual elements of an IC becomes restricted, which renders the characterization of these components difficult. Understanding the temperature distribution and thermal characteristics of a device is an important step in thermal management and improving device performance; in addition, thermal profiling can be used to extract material parameters and to characterize the optical performance of photonic ICs. Ultimately this knowledge can lead to better device designs and chip layouts.

Several thermography techniques have been used for temperature measurement of micrometre and sub-micrometre electronics and optoelectronic devices. Among them, infrared (IR) thermometry is perhaps the most widely used technique for temperature measurements of electronic devices, particularly ICs [2]. IR thermometry is based on determining

[8] Author to whom any correspondence should be addressed.
[9] Current address: Oxford Gene Technology, Oxford OX5 1PF, UK.
[10] Current address: Physical Sciences Inc., 20 New England Business Center, Andover, MA 01810, USA.

the spatial distribution of IR thermal radiation emitted from the surface of a solid [3, 4]. Based on Planck's law of blackbody radiation, the maximum spectral power density of an ideal blackbody at thermal equilibrium will shift to lower wavelengths with increasing temperature. Since, in practice the surface of a device under study is not a blackbody and reflects some of the incident radiation, the blackbody law must be scaled by a material dependent factor known as the emissivity ε. The total thermal radiation W integrated over the entire spectral range λ is given by $W = \varepsilon\sigma T^4$, where $\sigma = 5.7 \times 10^{-12}\,\mathrm{W\,cm^{-2}}$. Emissivity depends on the surface property and geometry, wavelength and temperature of the object, and must be known for each surface in order to obtain an accurate thermal profile. Silicon is largely transparent to near IR radiation, making IR thermography a valuable tool for thermal mapping of IC backplanes and hot spots. The thermal resolution of IR cameras (detectors) can be 10–20 mK, but their spatial resolution is mainly determined by the diffraction limit for the range of wavelengths to which the detector is sensitive. The most sensitive IR cameras work at 3 μm wavelength [3], which is ill-suited to the length scales of many modern electronic and optoelectronic devices. Use of a solid immersion lens can improve the resolution to sub-micrometre range, but low signal-to-noise ratios can still be a concern. Apart from the sub-optimal spatial resolution of IR thermography, other drawbacks include inaccuracy due to the attenuation of radiation between the target and the detector, uncertainty in the emissivity of the device surface and background radiation [4]. Furthermore, the low emissivity of metals, which are widely used as electrical contacts in devices, limits the application of IR thermography.

In the liquid crystal thermography (LCT) technique [3, 4], the surface of the device under study is covered with a thin layer of liquid crystal and illuminated with white light. At different temperatures, the liquid crystal layer reflects different wavelengths of this incident light. To improve the spatial resolution of the method, the nematic–isotropic phase transition of liquid crystal which occurs at the clearing point of the crystal, T_c, is used [5]. Below T_c the liquid crystal is in the nematic phase which scatters light and rotates the plane of polarization of the light and appears bright under a polarizing microscope. Above T_c, where the liquid crystal is in the isotropic phase, the plane of polarized light does not change and the image field appears dark. Taking advantage of the nematic–isotropic phase transition has given the LCT method a spatial resolution of 2–4 μm. The thermal resolution of LCT is approximately 0.1 K near the phase transition. Although LCT is less expensive than IR imaging, it is a semi-invasive technique and the thermal conductivity and heat capacity of the liquid crystal coating can affect the device under test. In addition, the uniformity and thickness of the liquid crystal layer are important factors in the accuracy and resolution of the technique [3].

Fluorescent micro-thermography (FMT) [6, 7] utilizes the temperature-dependent quantum efficiency of photoluminescent rare earth dyes. In this technique, the sample surface is coated with a thin film of such dyes and is then illuminated by ultraviolet (UV) light. FMT can be used for thermal imaging of electronic and bio sensing devices as well as hot spot detection and thermal mapping of ICs. A spatial resolution of 0.3 μm and a thermal resolution of 1 mK have been reported for FMT [4], although sample preparation and optical system design require special consideration. Photon shot noise, UV bleaching, film dilution and film preparation can have a significant impact on the quality of FMT thermal images.

Using micro-thermocouples as inexpensive point measurement contact probes can provide accurate temperature readings with a thermal resolution of 0.01 K. However, the large size of the thermocouple wires (~25–50 μm in diameter) results in a poor spatial resolution. In addition, difficulties in maintaining good thermal contact between the micro-thermocouple junction and the surface of a device can lead to erroneous readings. Finally, as point-based measurement tools, micro-thermocouples cannot be used for imaging without implementing complicated translation stages [3].

A thermography technique with very high spatial resolution is scanning thermal microscopy (SThM) which takes the use of micro-thermocouples to the nanometre scale. The SThM probe consists of a thermocouple fabricated on the tip of an AFM cantilever [8]. When the probe is scanned in contact mode over the surface of a sample, localized heat transfer between the sample surface and the probe tip leads to a change in the tip temperature that is measured by the thermocouple. In this way, both the tip–sample heat transfer across the entire surface and the sample topography can be obtained simultaneously with sub-micrometre spatial resolution (~0.05 μm) and a thermal resolution of 0.1 K [4]. However, the roughness of the sample surface can cause variations in the tip-surface thermal contact, leading to noise in the thermal signal. Furthermore, the SThM experimental setup is complicated and expensive, and data acquisition can be time-consuming due to the required scanning methods [3]. A major limitation of SThM is the liquid meniscus that forms between the tip and the sample, which is intrinsic to contact measurements done in atmosphere and limits the resolution of the technique. Finally, SThM cannot be used easily on light emitting surfaces of optoelectronic devices such as vertical cavity surface emitting lasers (VCSELs), because the light is absorbed by the SThM thermocouple and causes errors in temperature measurement [9].

In addition to the above-mentioned techniques, other methods of thermography include acoustic thermography [10], near-field scanning optical microscopy (NSOM) adapted for temperature measurement [11], Raman spectroscopy [12] and thermoreflectance microscopy. This final technique is the focus of this review and will be discussed in detail.

Thermoreflectance microscopy is based on measurement of the relative change in the reflectivity of a sample (device) surface as a function of change in temperature. As the temperature of the sample changes, the refractive index, and therefore the reflectivity, varies. The relation between the relative change in reflectivity and the temperature change can be approximated to first order as

$$\frac{\Delta R}{R} = \left(\frac{1}{R}\frac{\partial R}{\partial T}\right)\Delta T = \kappa \Delta T, \tag{1}$$

where κ, which is typically of the order of 10^{-2}–$10^{-5}\,\mathrm{K^{-1}}$, is the thermoreflectance calibration coefficient that depends

on the sample material, the wavelength of the illuminating light, the angle of incidence (and thus, by extension, the surface roughness) and the composition of the sample in the case of multi-layer structures.

Thermoreflectance spectroscopy has been used extensively since the 1960s to study the band structure and dielectric response functions of semiconductors [13]. As an imaging thermography technique, it has been utilized in point-based laser scanning methods [14], and with multi-point detection systems. For the latter, both non-CCD photodiode array-based systems [15], and CCD-based schemes have been applied to study thermal profiles of electronic and optoelectronic devices [16, 17]. Thermoreflectance has also been employed in pump–probe configuration to study phonon transport and the thermal relaxation of carriers on picosecond time scales [18]. Transient thermoreflectance (TTR) [19] and photomodulated thermoreflectance [20] have been used to characterize thermal diffusivity and other thermal properties of thin films.

It has been shown that the thermal and spatial resolutions of CCD-based thermoreflectance can be as low as 10 mK and 250 nm, respectively [21], but the fundamental temperature limit is not known yet. The high resolution of CCD-based thermoreflectance microscopy, its relatively short data acquisition times compared with other techniques and its suitability to a wide range of materials including metals and light emitting surfaces make it a leading method for studying thermal transport in electronic and optoelectronic devices under operating conditions. This technique is also applicable for studying thermal transients and heat transfer in thin films and low dimensional structures such as multilayers and superlattices [22].

In the following sections of this review, we present an overview of the physical basis of thermoreflectance, the most common experimental setup variations and signal processing and calibration techniques. We also review applications of CCD-based thermoreflectance microscopy in measuring temperature distributions of various devices.

2. Principles of thermoreflectance

Since the 1960s, optical modulation techniques have been used extensively to study the band structure of semiconductors at energies higher than the fundamental gap [13, 23–29]. In these techniques the response of the optical constants of a solid to a periodic change in a parameter such as electric field, pressure, temperature or wavelength of the incident radiation is measured [30]. The resulting spectra show well-resolved features stemming from critical points of the band structure that are isolated and separated from the background which is less sensitive to modulation.

A temperature increase creates a shift in the energy gap and also broadens the critical point involved. The shift of the energy gap involves two components, one due to thermal expansion and the other due to electron–phonon interaction. The thermal-expansion shift has the same sign as the phonon shift for most critical points observed, with comparable magnitude. The broadening is only due to the electron–phonon interaction, and is small compared with the total shift [13].

For non-magnetic, isotropic, homogeneous media, in which the optical constants can be treated as scalars, the phenomenological basis of thermoreflectance spectroscopy [30] can be understood by studying the change in the complex dielectric function $\hat{\varepsilon}(E) = \varepsilon_1(E) + \mathrm{i}\varepsilon_2(E)$, where ε_1 and ε_2 are the real and imaginary parts of the dielectric function, respectively, and E is energy.

The optical constant ε_2 is related to the band structure through the joint density of states function [29]:

$$\varepsilon_2(E) = \frac{4e^2\hbar^2}{\pi\mu^2E^2}\int \mathrm{d}\boldsymbol{k}|P_{\mathrm{cv}}(\boldsymbol{k})|^2\delta[E_{\mathrm{c}}(\boldsymbol{k}) - E_{\mathrm{v}}(\boldsymbol{k}) - E], \quad (2)$$

where μ is the combined density of states mass, the Dirac δ function represents the joint spectral density of states between the conduction (c) and valence (v) band states which differ by the energy $E_{\mathrm{c}}(\boldsymbol{k}) - E_{\mathrm{v}}(\boldsymbol{k}) = \hbar\omega$ of the incident light, $P_{\mathrm{cv}}(\boldsymbol{k})$ is the momentum matrix element between the conduction and valence band states, and the integration is performed over the first Brillouin zone.

The reflectivity R of the material for normal incidence of light has the form

$$R = \frac{(n-1)^2 + k^2}{(n+1)^2 + k^2}, \quad (3)$$

where n and k are the index of refraction and the extinction coefficient, respectively, and can be written as real and imaginary parts of the complex index of refraction $\hat{n} = n + \mathrm{i}k$. Since Maxwell's equations yield the relation $\hat{\varepsilon} = \hat{n}^2$, it follows that

$$\varepsilon_1 = n^2 - k^2, \quad (4a)$$

$$\varepsilon_2 = 2nk. \quad (4b)$$

Solving these equations for n and k, one obtains [30]

$$n = \left(\frac{(\varepsilon_1^2 + \varepsilon_2^2)^{1/2} + \varepsilon_1}{2}\right)^{1/2}, \quad (5a)$$

$$k = \left(\frac{(\varepsilon_1^2 + \varepsilon_2^2)^{1/2} - \varepsilon_1}{2}\right)^{1/2}. \quad (5b)$$

In thermoreflectance spectroscopy experiments, it is the relative change in reflectivity ($\Delta R/R$), resulting from the modulation of temperature, which is measured. The contributions of n and k to the modulated reflectance can be obtained by differentiating (3), yielding

$$\frac{\Delta R}{R} = \frac{4(n^2 - k^2 - 1)\Delta n + 8nk\Delta k}{[(n+1)^2 + k^2][(n-1)^2 + k^2]}, \quad (6)$$

where Δn and Δk are the changes in n and k resulting from the modulation. Substituting (5*a*) and (5*b*) into (6) yields

$$\frac{\Delta R}{R} = \alpha(\varepsilon_1, \varepsilon_2)\Delta\varepsilon_1 + \beta(\varepsilon_1, \varepsilon_2)\Delta\varepsilon_2, \quad (7)$$

with

$$\alpha = \frac{2A}{A^2 + B^2}, \tag{8a}$$

$$\beta = \frac{2B}{A^2 + B^2}, \tag{8b}$$

where

$$A = n(n^2 - 3k^2 - 1), \tag{9a}$$

$$B = k(3n^2 - k^2 - 1). \tag{9b}$$

The coefficients α and β, which are functions of n and k and thus the photon energy, weight the contributions of $\Delta\varepsilon_1$ and $\Delta\varepsilon_2$ to the modulated reflectance, respectively. Their signs and magnitudes determine the response in different spectral regions, and have been derived for electroreflectance analysis [31]. It should be noted that $\varepsilon_1(\omega)$ and $\varepsilon_2(\omega)$, and therefore their modulations, are not independent and are related explicitly by the Kramers–Kronig transformation. According to this relation, the temperature induced change in $\varepsilon_2(\omega)$ causes a related change in $\varepsilon_1(\omega)$, given by

$$\Delta\varepsilon_1(\omega) = \frac{2}{\pi} P \int_0^\infty \frac{\omega' \Delta\varepsilon_2(\omega')}{\omega'^2 - \omega^2} \, \mathrm{d}\omega', \tag{10}$$

where P denotes the principal value of the integral.

If $\Delta\varepsilon_1$ and $\Delta\varepsilon_2$ can be calculated from some suitable theory as a function of change in temperature, then the theoretical thermoreflectance spectrum of $\Delta R/R$ can be obtained via (7). An interpretation is possible if an agreement between experimental and theoretical spectra exists.

As mentioned earlier, the temperature increase causes a shift in the energy gap and broadens the critical point involved. Combining these two effects, one can write

$$\Delta\hat{\varepsilon} = \frac{\mathrm{d}\hat{\varepsilon}}{\mathrm{d}E_\mathrm{g}} \frac{\mathrm{d}E_\mathrm{g}}{\mathrm{d}T} \Delta T + \frac{\mathrm{d}\hat{\varepsilon}}{\mathrm{d}\Gamma} \frac{\mathrm{d}\Gamma}{\mathrm{d}T} \Delta T, \tag{11}$$

where E_g is the energy gap and the broadening is accounted for, phenomenologically, by the broadening parameter Γ. Near the fundamental absorption edge of the semiconductor, it can be found approximately that [30]

$$\Delta\varepsilon_1 \propto -\frac{1}{\Gamma} \left(\frac{1}{x^2 + 1} \frac{\mathrm{d}\Gamma}{\mathrm{d}T} - \frac{x}{x^2 + 1} \frac{\mathrm{d}E_0}{\mathrm{d}T} \right) \Delta T, \tag{12a}$$

$$\Delta\varepsilon_2 \propto -\frac{1}{\Gamma} \left(\frac{x}{x^2 + 1} \frac{\mathrm{d}\Gamma}{\mathrm{d}T} + \frac{1}{x^2 + 1} \frac{\mathrm{d}E_0}{\mathrm{d}T} \right) \Delta T, \tag{12b}$$

where $x = (\hbar\omega - E_0)/\Gamma$ and E_0 is the inter-band energy at the critical point. When the broadening parameter is assumed to be constant ($\mathrm{d}\Gamma/\mathrm{d}T = 0$), the thermoreflectance spectrum is simply the first derivative with respect to the optical frequency of the joint electronic density of states in (2). For this reason, thermoreflectance is referred to as a first-order modulation spectroscopy (as opposed to electroreflectance, which is a third-order modulation spectroscopy).

While thermoreflectance spectroscopy is a powerful tool for studying the band structure and dielectric response function of semiconductors, here we focus on its application in thermography as described by (1) in which all of the effects of the material's reflectance modulation are lumped into the thermoreflectance calibration coefficient κ (λ). Because κ (λ) can vary sharply within the spectral region of interest (often the visible spectrum), the choice of illumination wavelength determines not only the spatial resolution of the technique but also the sensitivity [32]. For most metals and semiconductors, the thermoreflectance coefficient is only in the range of 10^{-5}–$10^{-2}\,\mathrm{K}^{-1}$. Therefore, for most practical applications, a highly sensitive measurement is required to obtain quantitative information about the temperature of the device under test.

The change in reflectance of the material under study can also result from modulation induced changes other than the temperature change. For example, in semiconductor lasers and amplifiers, the change in carrier density, as a result of change in device bias, can alter the index of refraction. The subsequent change in reflectivity combines with that due to temperature change, potentially complicating interpretation of the results [33].

3. Experimental setup

The development of thermoreflectance as a thermography tool has mainly focused on two realizations: point measurements and CCD-based measurements [16]. In the former, a focused laser beam is used as the illumination source and a single element photodiode, coupled with a lock-in amplifier, is used as the detector. The sample is usually placed on a translation stage and the measurement is made for each point. Scanning the sample surface with the laser beam provides the thermal image. This technique has a very high sensitivity and is capable of detecting relative changes in reflectivity less than $\Delta R/R = 10^{-6}$. The disadvantage of this method is that it is time consuming with a typical 500×500 pixel scanned image requiring approximately an hour to acquire.

Various improvements have been employed to reduce the acquisition time in laser scanning thermoreflectance, without loss of sensitivity. In one such case, a photodiode array with synchronous multiple point bandwidth filtering is used as the basis for a thermal imaging microscope [15]. This state-of-the-art diode array camera achieves thermoreflectance imaging with 10 mK resolution in 1 s, while by combining multiple frames, a spatially enhanced image can be obtained in minutes [3]. The photodiode array camera has a higher dynamic range and sensitivity than a CCD camera, because each diode in the array is ac-coupled with an analog amplifier and a precision 24-bit, 40 kHz, analog–digital (A/D) converter. The ac coupling at each pixel allows the signal to be boosted without saturation of the dc component. Such performance, however, greatly increases system complexity; current versions of the system include only 16×16 pixels, much fewer than a standard CCD.

Another improvement upon laser scanning thermoreflectance has been achieved by using a fast scanner made of two galvanometric mirrors, which sweeps a focused laser beam across the device [34]. This method has achieved a spatial resolution of the order of the diffraction limit (~300 nm), which is comparable to that attained by CCD-based thermoreflectance, and a $\Delta R/R$ resolution of 10^{-5}. One limitation of this setup is the range of the temperature modulation frequency, which is

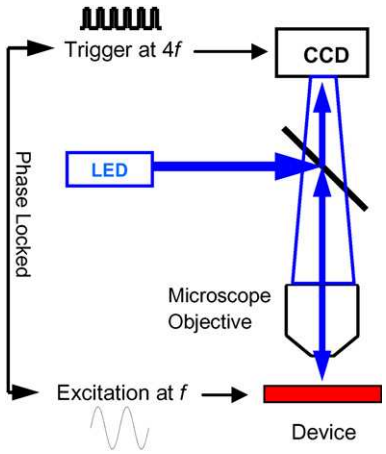

Figure 1. Schematic depiction of a homodyne thermoreflectance microscopy setup.

on the order of a few tens of kilohertz. This can be a drawback because the temperature variation amplitude of the thermal modulation decreases as the frequency increases.

The basic experimental setup for a high spatial-resolution CCD-based thermoreflectance is shown in figure 1. The setup consists of a visible light CCD camera and a light emitting diode (LED) illumination source that is focused onto the sample by a microscope objective [16]. The light reflected back to the CCD in response to modulation of the sample temperature is then analysed by a computer. The use of an incoherent light source (LED) instead of a focused laser beam eliminates speckle or fringe type interference patterns that may occur with coherent illumination. Various modulation schemes can be used to detect the relative change in reflectivity of the sample surface, including the homodyne method, the heterodyne method and the techniques for studying transients, as described below.

Recognizing that the thermoreflectance coefficient κ is strongly dependent on the probe wavelength, the $\Delta R/R$ response is significantly enhanced near the wavelengths where $\mathrm{d}R/\mathrm{d}T$ has a maximum value and the reflectivity R is minimum (see (1)). Therefore, the choice of probe wavelength plays an important role in determining the sensitivity of CCD-based thermoreflectance.

3.1. Homodyne technique

In the homodyne technique, the temperature of the sample is modulated using a signal generator that is phase-locked to the CCD frame trigger, and the LED illumination is in the continuous wave (CW) mode. The modulation frequency of the sample temperature is f, which also implies a modulation of reflectivity at the same frequency

$$R(x, y, t) = R_0(x, y, t) + \Delta R(x, y, t)\cos(2\pi f t + \varphi(x, y) + \psi), \tag{13}$$

where $\varphi(x, y)$ is the phase shift due to the thermal modulation and ψ is an arbitrary uniform phase shift accounting for any overall delay between the modulation signal and the camera trigger [21]. Using a multichannel lock-in scheme and triggering the camera at a frequency of $f_c = 4f$, a 2D image can be obtained that represents the modulated reflectivity $\Delta R(x, y)$, and through a calibration, the modulated temperature $\Delta T(x, y)$. Choosing f_c to be four times the frequency of temperature modulation causes the camera to take four images during each period T of the temperature modulation, with these images corresponding to the following four integrals [16]:

$$I_1 = \int_0^{T/4} R(x, y, t)\mathrm{d}t, \qquad I_2 = \int_{T/4}^{T/2} R(x, y, t)\,\mathrm{d}t,$$
$$I_3 = \int_{T/2}^{3T/4} R(x, y, t)\mathrm{d}t, \qquad I_4 = \int_{3T/4}^{T} R(x, y, t)\,\mathrm{d}t, \tag{14}$$

The modulation amplitude $\Delta R(x, y)$, the dc image $R_0(x, y)$ and the relative phase $\varphi(x, y)+\psi$ can then be obtained through the following relations:

$$\Delta R(x, y) = \frac{4\pi}{\sqrt{2}T}\sqrt{(I_1 - I_3)^2 + (I_2 - I_4)^2},$$
$$R_0(x, y) = \frac{2}{T}(I_1 + I_2 + I_3 + I_4), \tag{15}$$
$$\varphi(x, y) + \psi = \frac{2}{\pi}\arctan\frac{I_1 + I_2 - I_3 - I_4}{I_1 - I_2 - I_3 + I_4}.$$

The normalization of the modulated signal by the dc signal allows extraction of the relative change in reflectivity described in (1):

$$\frac{\Delta R(x, y)}{R_0(x, y)} = \sqrt{2}\pi\,\frac{\sqrt{(I_1 - I_3)^2 + (I_2 - I_4)^2}}{I_1 + I_2 + I_3 + I_4} \tag{16}$$

This lock-in measurement technique (which is sometimes referred to as the 'four bucket' technique), makes best use of the CCD array's slow readout speed by simply accumulating a number of identically phased images in each bin (I_1, I_2, I_3 or I_4) and recording a cumulative average of the contents. Thus, even if many images are captured (increasing the sensitivity of the technique), only four image buffers (one for each phase bin) need be kept in memory throughout the procedure [33].

3.1.1. Signal processing and noise analysis. Since the thermoreflectance coefficient of some materials over accessible wavelengths can be quite low (e.g. $10^{-5}\,\mathrm{K}^{-1}$), it is important to consider whether the CCD approach has the required sensitivity for imaging small (<1 K) changes in temperature. For example, without boosting the resolution of the camera using this averaging, the thermal resolution for a typical thermoreflectance measurement would be at most $\kappa^{-1}/2^b$, where κ is the thermoreflectance coefficient and b is the bit depth of the camera. For a material with $\kappa = 1 \times 10^{-4}\,\mathrm{K}^{-1}$ and for a typical camera with $b = 12$, this worst-case resolution is approximately 2.5 K. However, for a wide range of practical measurement scenarios, the shot noise present in the incident photons and the thermal noise present at the input of the A/D converter can provide a sufficient amount of dither to resolve sub-quantization level

temperatures via the phenomenon sometimes referred to as 'stochastic resonance' [35].

Lüerßen *et al*, provide empirical evidence for 10 mK temperature resolution on a gold surface, using an illumination wavelength optimized for the material [36]. This corresponds to an equivalent bit depth of 18 bits rather than the 12 bits offered nominally by the camera. This extra resolution results from the repeated averaging of the quantized signal in the presence of a sufficiently large noise, which causes the camera pixel's signal to switch between adjacent quantization levels.

In order to obtain sub-quantization level thermal images, averaging must be performed over many images. Mayer *et al* [21] have analysed the number of iterations required to achieve a given temperature resolution (and the specific form of the convergence) by propagating the approximately Gaussian fundamental noise sources (thermal or shot noise) present at the input of the measurement through the signal processing chain. They constructed an estimator of the temperature fluctuation present in the sample based on the observable reflected light and the various measurement parameters which impact the accuracy of the measurement including the depth of the thermal and reflectance modulation, the mean level of reflected light, the number of iterations (thermal cycles) that are averaged over and the intrinsic noise present in a pixel (thermal, shot or quantization noise). The estimator takes the form of a Rice distribution. By taking the difference of the estimator with respect to the true thermal signal and the standard deviation of the estimator, the dependence of the thermoreflectance error as a function of the measurement conditions can be found. The errors in both the first moment (mean) and the second moment (variance) decrease as average signal level and the number of iterations increase. The errors also decrease as the fundamental noise sources at the pixel decrease, provided that sufficient noise is present to bump the signal between different quantization bins of the analogue to digital (A/D) converter in the camera.

This can be used to plan measurements and make a statistical prediction of a measurement's accuracy; alternatively, the measurement can simply be run until the value of the thermoreflectance is converged, since it is shown that for sufficient averaging the thermoreflectance estimator is unbiased [21]. A useful and intuitive result of the detailed analysis is that in the limit of a small thermoreflectance signal the accuracy of the measurement (the standard deviation) scales as $1/\sqrt{N}$, where N is the number of thermal oscillations measured (i.e. the amount of averages taken). Hence, to double the accuracy of the measurement, it must typically be run for four times as long.

The model of [21] was experimentally confirmed by performing sub-quantization threshold imaging of a diffused resistor in a Si wafer. Mayer *et al* [33] further discussed the conditions required for stochastic resonance, the optimal noise signal size ($\sim 1/2$ LSB of the A/D converter), the impact of quantization noise and the functional form of both the magnitude and phase probability distribution functions (PDFs) as a function of the measurement and system variables. The ultimate temperature resolution using this method is set by the ideality (integral and differential non-linearity) of the A/D converter. This was illustrated using a Monte Carlo analysis [21]. Using this method of averaging, the discrete limit for the 12-bit system can be lowered to $\Delta R/R = 2.5 \times 10^{-6}$ and possibly beyond, with a corresponding expansion in dynamic range from 72 to 114 dB. Combined with appropriate selection of illumination wavelength, stochastic resonance CCD systems have achieved thermal resolution of 10 mK and spatial resolution of 250 nm [21].

The homodyne thermoreflectance techniques are suitable for obtaining thermal images of low-frequency phenomena, since the frequency of temperature modulation is limited by the frame rate of the CCD camera. In order to image high-frequency thermal phenomena, a modification of the homodyne technique has been developed by Grauby *et al* [16] as discussed in the next section.

3.2. Heterodyne technique

In this method, the temperature (and reflectivity) of the sample is modulated with a frequency f_1, as in (13) and LED illumination is modulated at a slightly different frequency f_2, with its flux given by

$$\phi(t) = \frac{\phi_1}{2}[1 + \cos(2\pi f_2 t)]. \tag{17}$$

Using the same multichannel lock-in scheme as in the homodyne method, the slow difference frequency $F = f_2 - f_1$ component of the reflected signal can be detected by triggering the camera at a frequency $f_c = 4F$; the flux reflected back to the camera can be written as

$$s(x, y, t) = \frac{\phi_1}{2} R_0(x, y, t) + \frac{\phi_1}{4} \Delta R(x, y, t) \cos[2\pi F t - \varphi(x, y) - \psi]. \tag{18}$$

For example, if the sample temperature is to be modulated at $f_1 = 1$ MHz, then with the LED modulated at $f_2 = 1$ MHz + 10 Hz, the blinking term $F = f_2 - f_1$ is only 10 Hz, and the camera can be easily triggered at $4F = 40$ Hz. Synchronization between the camera control, LED and device heating can be achieved using a phase-locked system and synchronous counters. Grauby *et al* have used this method to obtain amplitude and phase images of the Joule and Peltier heat exchange in a polycrystalline silicon resistor [16].

3.3. Transient thermal imaging using thermoreflectance

In both of the above frequency domain measurement techniques, a lock-in method captures the steady-state thermal signal but provides limited information about thermal transients. However, it is often desirable to observe how devices thermally evolve in time. Due to the size of typical electronic and optoelectronic devices, thermal effects can occur on a millisecond or microsecond time scale or faster.

Thermoreflectance methods based on time domain analysis can characterize fast transient heating effects such as the thermal rise time by reconstructing the time varying reflectance signal. While CCD frame rates are typically much slower than device thermal time constants, single point TTR

can be performed using a focused laser spot as a probe and fast PIN photodetector coupled into an oscilloscope which can monitor the surface reflectivity. Time resolution is determined by the response of the photodetector or the oscilloscope sampling period, whichever is slower. Combined with a scanning mechanism, 2D images of fast thermal transient patterns for devices have been recorded with 20 ns time resolution [37]. While the signal-to-noise ratio in such systems is impressive, they have drawbacks in measurement time and expense.

In order to partially overcome the slow frame rates associated with CCDs, Maize *et al* [38] have used a pulsed LED and a CCD camera to acquire transient thermal images almost 100 times faster than single point TTR, without the need for a laser and scanning translation stage. Their technique utilizes a pulsed boxcar averaging scheme in which the boxcar average is combined with a short duration LED pulse (∼10 ns) synchronized with device excitation. For each exposure of the CCD, there is one LED pulse, effectively reducing the camera exposure to the time duration of the LED pulse width. For the next integration period of the CCD, the phase between the LED pulse and the device excitation is advanced by a small, known amount, and the in-between data points are filled in by combining multiple boxcar averages. By stepping the light pulse in regular increments, the CCD thus records the full thermal transient of the device with time resolution limited by the pulse width. This method has been used to demonstrate transient thermal imaging of a micro-heater with millisecond and microsecond time resolution, comparing rapid heat diffusion in the device metal to slower diffusion into the substrate [38].

4. Calibration techniques

As mentioned earlier, the thermoreflectance coefficient κ depends strongly on the material of the sample under test and the illumination wavelength. Both material and illumination wavelength play an important role in determining R and $\mathrm{d}R/\mathrm{d}T$ [32]. In addition, electronic devices often studied with this technique usually have layered structures that strongly modify the thermoreflectance coefficient. Therefore, in order to maximize the sensitivity of CCD-based thermoreflectance measurements, it is crucial to determine the best illumination wavelength(s) for each material under investigation. As the photothermal response differs strongly from one material to another, it is in principle necessary to repeat this process for each material under study.

One way to calibrate thermoreflectance for a range of wavelengths is to use different LEDs as illumination sources, and measure the photothermal response at each LED wavelength. This has been demonstrated on a 45 nm thick NiCr oxide resistor deposited on a GaAs substrate with 1.5 μm thick Au Ohmic contacts and blanked coated with a Si_3N_4 passivation layer [39]. Red LEDs ($\lambda = 615$ and 660 nm) exhibited low response for both bare and passivated Au, while an orange LED ($\lambda = 598$ nm), as depicted in figure 2, was shown to be suitable for thermal imaging of passivated NiCr and Au. Green illumination ($\lambda = 511$ nm) gave a large signal

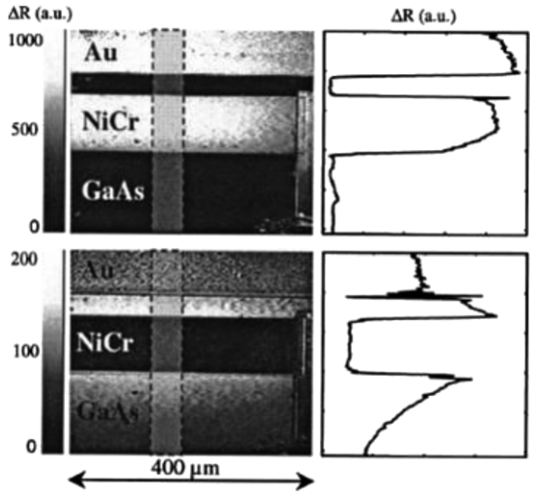

Figure 2. Reflectivity change (ΔR) images of a 45 nm thick NiCr oxide resistor deposited on GaAs substrate with Au Ohmic contacts, coated with Si_3N_4 passivation layer at illumination wavelengths $\lambda = 598$ nm (top) and $\lambda = 511$ nm (bottom). The profiles on the right show the values of ΔR averaged over the greyed area of the images. (Reprinted with permission from [39]. Copyright 2001 American Institute of Physics.)

for Si_3N_4-coated GaAs and a small signal for passivated Au (figure 2). Therefore, it is possible to measure the thermal behaviour of a selected material within a complex structure by careful choice of the illumination wavelength.

The method of using different LEDs to enhance signal sensitivity in thermoreflectance calibration is time consuming because of the number of images that have to be acquired at each LED wavelength; this also increases the risk of drift. Another approach has been developed [40] in which a thin line-shaped region of the sample is illuminated with a beam of white light from a slit. The back reflected light from the sample is then spectrally dispersed on a CCD using a grating, with a glass prism used to realign the first-order diffraction with the optical axis. A schematic of this method is shown in figure 3. It has been shown that a spectral range of $\Delta\lambda = 200$ nm with a few nanometres resolution can be achieved in this way, and with two acquisition the entire visible spectrum can be sampled. By also measuring the temperature modulation amplitude ΔT (e.g. by using a micro-thermocouple), the acquisition system can then be used to obtain R or $\mathrm{d}R/\mathrm{d}T$ for a wide spectrum. Although the spectral response of CCDs is not flat in the visible range, it can be calibrated using a mirror of known reflectivity to obtain accurate quantitative values for $R(\lambda)$ and $\mathrm{d}R/\mathrm{d}T(\lambda)$ [40].

The calibration procedure, namely determination of thermoreflectance coefficient κ, can be performed with the carefully chosen illumination wavelength using micro-thermocouples. By placing a thermocouple (which usually has a diameter of the order of 25 μm) on a chosen region of the sample and using a low modulation frequency (which guarantees that the thermal diffusion length is much larger than the layer thickness), the variations of the temperature ΔT can be directly measured in or near the area sampled by thermoreflectance. By acquiring a simultaneous thermal image under the same conditions, it is then possible to

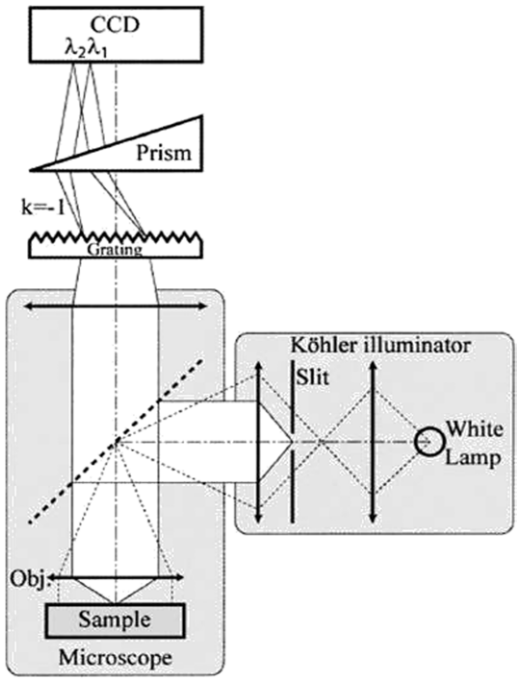

Figure 3. Modified microscope for the measurement of the reflectivity as a function of wavelength $R(\lambda)$. (Reprinted with permission from [40]. Copyright 2003 American Institute of Physics.)

measure the relative change in reflectivity $\Delta R/R$ of this area. By repeating this measurement at different amplitudes of temperature modulation, a linear relation between $\Delta R/R$ and ΔT can be obtained, for which the slope determines the thermoreflectance coefficient κ.

It is evident, therefore, that in order to determine κ two different experimental methods are involved that can, in general, have different constraints and preferred measurement conditions. The thermal calibration might be performed using a micro-thermocouple and lock-in amplifier to measure only the time-varying changes in voltage, while the optical measurements might be carried out using a CCD camera. These methods have different practical ranges for frequency. Micro-thermocouples are better suited for low-frequency measurements since thermal equilibrium with the sample has to be established; as a consequence, there is a frequency above which one can observe a roll over of the voltage. For example, a roll-over frequency of approximately 3 Hz was measured for type-T micro-thermocouple made from AWG42 copper–constantan wires [41]. CCD measurements, on the other hand, benefit from short exposure times, as this decreases the thermal noise in the detector. Exposure times larger than a few hundred milliseconds require active cooling of the detector if the signal is not to be dominated by thermal noise; in other words, the lowest reasonable frequency of the modulation in homodyne detection is on the order of about 10 Hz.

The heterodyne measurement setup [16], which was developed to be used for high thermal modulation frequencies (see section 3.2), can be utilized to improve thermoreflectance calibration. A low frequency f_1 can be used for the thermal modulation of the device under calibration in order to facilitate micro-thermocouple measurements, while a higher illumination frequency f_2 is used to detect the signal on the sum frequency [42]. However, this presents practical constraints for the frequency selection compared with the high-frequency application. One of the considerations is the frequency rejection of the lock-in detection scheme implemented with the CCD camera; for example, if the required thermal modulation frequency is 1 Hz, then the frequency discrimination of the lock-in setup needs to be better than this. The measurement of the rejection window is easily done; e.g. by using a homodyne measurement in which the detection frequency is kept constant and the thermal modulation frequency is varied around the detection frequency in order to observe the width of the response curve.

It should also be noted that imperfections of the thermocouple junction and poor thermal contact between the junction and the sample surface can lead to a measured temperature that is lower than the actual surface temperature. At low frequencies, micro-thermocouples should give a reasonable value for ΔT; improvements are possible using a Peltier element and thermistor to control the temperature of the whole device in a feedback loop [9, 43].

Since thermoreflectance imaging measurements are typically performed at normal light incidence, thermal expansion or contraction of the device under study does not cause significant deflection of the light at low magnification. However, at higher magnification conditions, vertical movement of the sample can cause defocusing and loss of information. It has been shown [44] that for a microscope objective with a numerical aperture (NA) of 0.8, the image intensity and measured thermoreflectance of a sample that moves up or down by 300 nm relative to the focal plane of the microscope will change by 5×10^{-4} due to the changing amount of collected light. The relative variation of the reflected signal as a function of the sample position is parabolic. A lateral displacement caused by inhomogeneous expansion has also been observed for magnifications higher than 20× which should be accounted for when measuring the reflectivity of a chosen region of the sample [43].

The microscope objective has also some influence on the value of the calibration coefficient. The main effect is induced by NA, since both R and $\partial R/\partial T$ are strongly dependent on the angle of incidence in situations where optical interference occurs in encapsulated layers, such as in ICs. It has been observed [43] that lower NA yields sharper spectral features, whereas higher values give smoother responses since a wider range of angles of incidence are averaged. For example, it has been shown that the thermoreflectance coefficient of polycrystalline Si is changed from $+4.3 \times 10^{-4}\,\mathrm{K}^{-1}$ at 0.4 NA to $-2.2 \times 10^{-3}\,\mathrm{K}^{-1}$ at 0.8 NA. Therefore, it is important to perform the calibration and thermoreflectance measurements with the same microscope objective [43].

5. Applications of CCD-based thermoreflectance microscopy

In this section we review some of the applications of CCD-based thermoreflectance technique in hot spot detection,

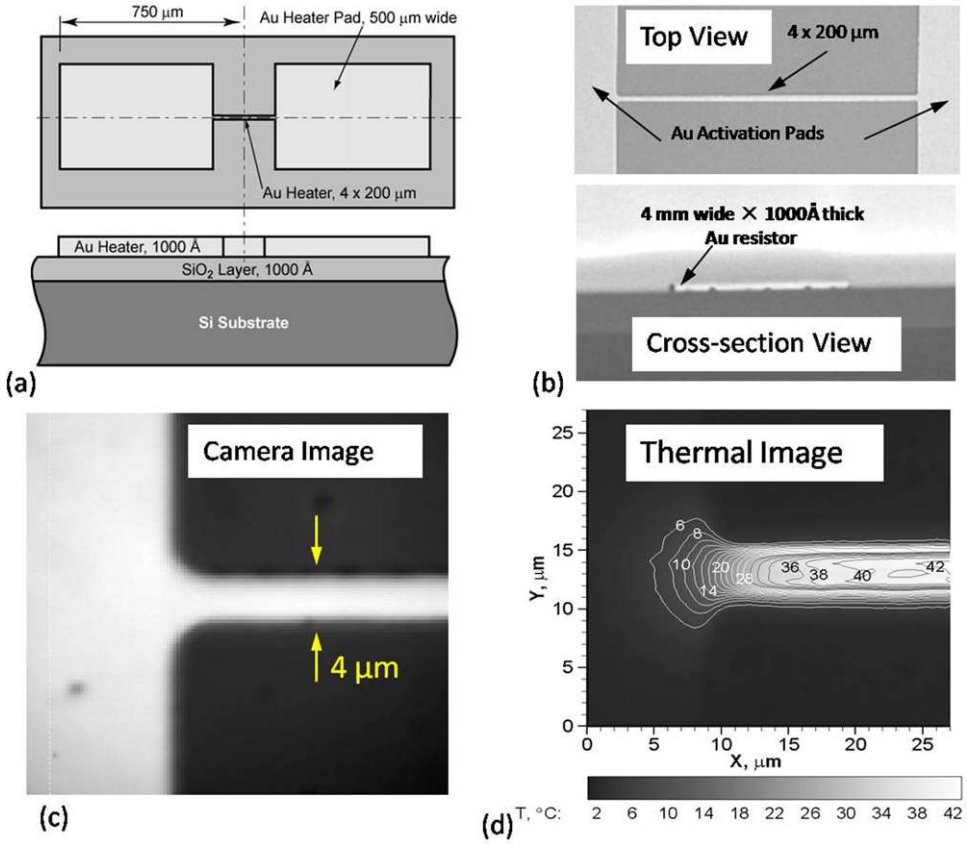

Figure 4. (*a*) Schematic, (*b*) cross-section view, (*c*) scanned area of device and (*d*) corresponding temperature contours on an activated gold resistor device at instant of peak temperature: illumination at 0.485 μm; magnification = 75×; spot size = 0.21 μm; power = 97 mW. The thermal image in part (*d*) results from averaging over about 1000 heating cycles. (Reprinted with permission from [46]. Copyright 2006 THERMINIC.)

thermal mapping and thermal transient studies of various electronic and optoelectronic devices, including ICs.

5.1. Hot spot detection in electronic devices

Perhaps the most straightforward application of CCD-based thermoreflectance microscopy is in the detection of hot spots that can occur in a variety of microelectronic and optoelectronic devices. Because these hot spots can indicate a defect or catastrophic failure in the device, a non-invasive detection technique with high spatial resolution can be a valuable tool.

The application of CCD-based thermoreflectance imaging in detecting hot spots has been demonstrated [45] on transistor arrays with defect-induced leakage. The defects were identified on the thermal images as hot spots after a very short acquisition time with a spatial resolution of 350 nm.

5.2. Resistors

CCD-based thermography can further be used to acquire the surface temperature profiles of micro-scale resistors. The first heterodyne CCD-based thermal images were demonstrated by Grauby *et al* [16] using a polycrystalline Si resistor array. Thermoreflectance amplitude and phase images of the resistors were obtained by modulating the resistors' applied voltage at $f = 1$ MHz. To investigate the Joule heating effect (which has a magnitude of V^2/R and therefore is expected to occur at $2f$), the LED was modulated at a frequency of 2 MHz + 10 Hz, with a camera trigger at 40 Hz. The thermoreflectance amplitude showed a quadratic behaviour as a function of the applied voltage, as expected. By modulating the LED at 1 MHz + 10 Hz, a linear amplitude versus applied voltage was obtained, indicating the thermoelectric Peltier effect. These measurements show that, by varying the frequency of detection, CCD-based thermoreflectance is capable of distinguishing between the Joule and Peltier effects.

Figure 4 shows another example of thermoreflectance imaging, in this case applied to map the surface temperature of a 4 μm wide gold micro-resistor [46]. The top and cross-sectional images of the micro-resistor shown in figure 4(*b*) were obtained by use of a focused ion beam (FEI FIB-205) system and an electron microprobe (JEOL JXA-733 Superprobe). An optical image of the scanned area of the device and an example of the temperature contours measured with the CCD thermography system are shown in figures 4(*c*) and (*d*), respectively.

Thermoreflectance imaging has also been used to map temperature variations of a microelectromechanical system (MEMS) consisting of a loop-shaped, phosphorous-doped polysilicon resistive heater (13.3 kΩ) supported by a thin (<1 μm) dielectric membrane made of SiO_2 and Si_3N_4.

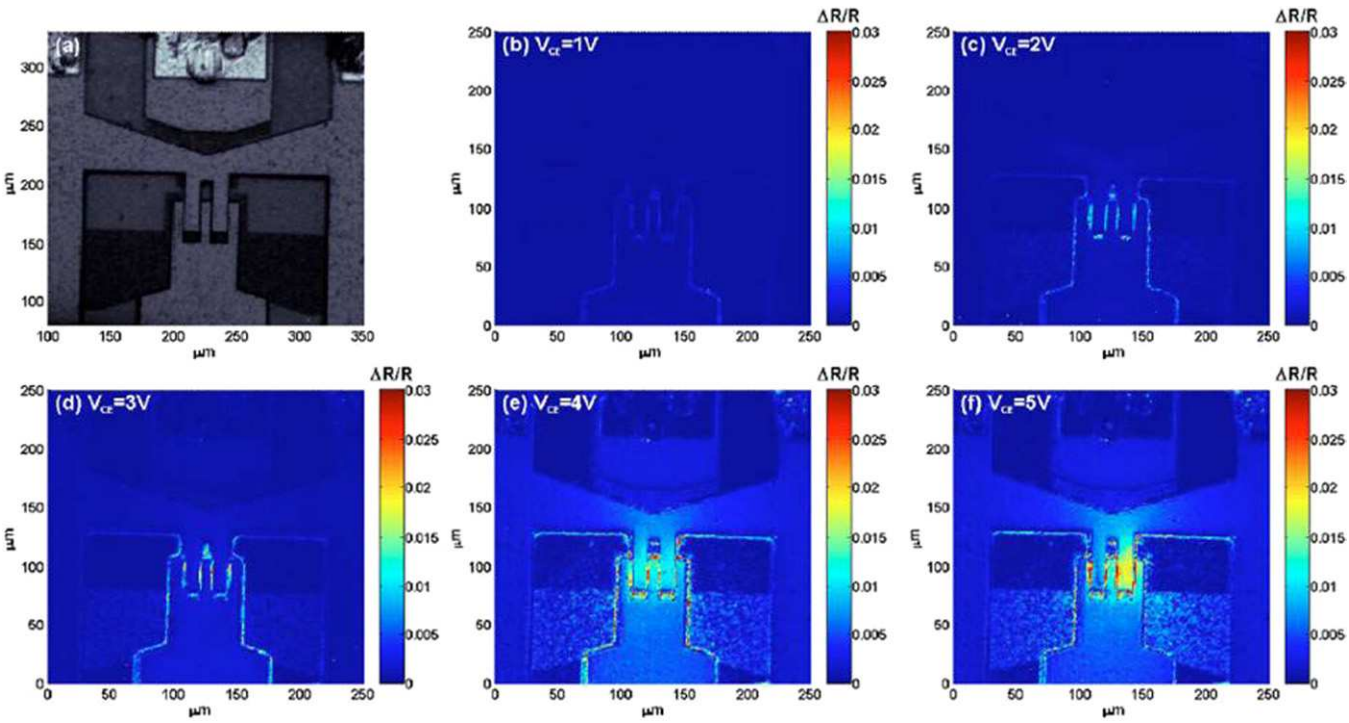

Figure 5. Profiling current density in high-power transistors: normalized thermoreflectance images ($\Delta R/R$) of a SiGe HBT at increasing V_{CE} bias with V_{BE} held constant at 1.52 V. The thermal images result from about an hour total accumulation time. (Reprinted with permission from [48]. Copyright 2006 American Institute of Physics.)

Calibration of the resistor was carried out by first determining the resistance as a function of temperature in an oven and then calibrating the resistance as a function of dissipated power from current–voltage measurements. From these measurements, a temperature variation versus power can be deduced. By measuring thermoreflectance signals ($\Delta R/R$) for a given dissipated power, the thermoreflectance calibration coefficient, $(\Delta R/R)/\Delta T$, was obtained for both the resistor and the dielectric layers [47].

5.3. Thermal mapping in electronic and microelectronic devices

5.3.1. Transistors. Utilizing the link between current density and temperature, high-resolution thermal microscopy has been used as a non-destructive tool to image current density in high power heterojunction bipolar transistors (HBTs) [48]. As shown in figure 5, this technique can be used to quantify effects such as current hogging in subcells of multifinger power transistors, a primary cause of reduced overall gain and device failure.

5.3.2. Micro-refrigerators on a chip. Figure 6 shows thermoreflectance images of a $40 \times 40\,\mu m^2$ heterostructure integrated thermionic (HIT) micro-cooler [3]. The images were acquired using a 14-bit 128×128 pixel enhanced CCD camera from Andor technologies. Multiple frames containing time series thermoreflectance data are recorded and thermal and phase images are extracted using fast Fourier transform and boxcar averaging. Illumination with a 455 nm blue LED was chosen to maximize thermoreflectance on the micro-cooler's gold surface (figure 6(*a*)). One hundred boxcar averages of a 1 s time series (340 frames) yields temperature resolution down to 50 mK. Figure 6(*b*) shows the CCD thermal image of the micro-cooler biased to 250 mA, calibrated for the gold region. Figure 6(*c*) shows the relative phase of the periodic thermal signal at different points on the micro-cooler sample surface. Measurement has shown that the substrate material and the gold have opposite sign thermoreflectance coefficients at 455 nm. This is represented by a thermal phase shift at the micro-cooler's perimeter where gold transitions to the substrate, indicating that device cooling extends a few micrometres into the substrate.

5.3.3. Electronic ICs. By combining the thermal maps obtained experimentally with the numerical simulation it is proven that several novel problems such as determining the thermal conductivity of new materials [49], finding the actual geometric parameters of an electronic device [50] and determining the power distribution in a device [51] can be addressed.

An example of solving a complex problem is described in [50]. In this work the thickness of a SiO_2 passivation layer as well as the geometrical dimension of a buried metal resistor in a set of micro-heater devices have been determined by combining the surface temperature map of the device, obtained by CCD-based thermoreflectance thermography, with a computational engine. In this way it has become possible to use the independent information from the experimental measurements to mitigate the lack of knowledge in the critical model parameters, which directly affect the usefulness of the

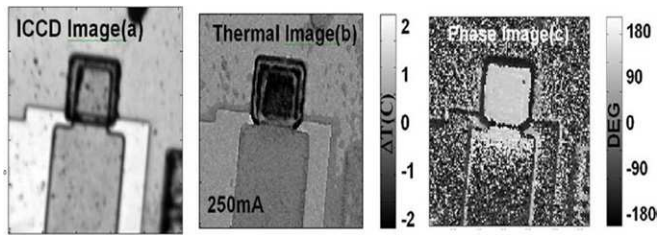

Figure 6. Thermoreflectance imaging using a CCD camera. (*a*) Blue LED microscope image of a $40\times40\,\mu m^2$ integrated micro-cooler. (*b*) Thermoreflectance temperature amplitude image and (*c*) phase image of the micro-cooler at 250 mA bias. The thermal image results from averaging over 25 000 heating cycles (about 15 min of total accumulation time). (Reprinted with permission from [3]. Copyright 2003 ASME.)

computational results. In this method, first the transient two-dimensional surface temperature is measured by the use of the thermoreflectance thermography system [46]. Then the inverse heat transfer problem is solved using the self-adaptive ultra-fast numerical technique [52]. The result is the three-dimensional thermal behaviour of multi-layered ICs (with embedded features). To minimize the number of uncertainty sources that the inverse method must deal with, the thermo-physical properties of the various thin layers are measured independently with the TTR technique [53].

Several experimentally obtained and the corresponding 'matched' (numerically obtained) surface temperature contours are shown in figure 7. It can be seen from this figure that there is a monotonic behaviour in the variation of the length of the heat source versus its width. Specifically, the length of the heat source increases with the increase in the width of the device as depicted in figure 7. This can be explained based on the fact that the end effect is more pronounced in the wider heating strips and therefore the computational model (which does not include any special treatment to simulate the end effects) becomes less realistic. This fact is more evident from analysing the data shown in figure 7. When examining data representing the experimental and numerically matched temperature profile across and along the heater (figure 7(*c*)), it is clear that the end effects are more pronounced for the 50 μm heater as compared with the 14 μm, while the 26 μm falls in between the two.

In another application of CCD-based thermoreflectance microscopy for temperature measurements in electronic ICs, Tessier *et al* [43] have studied a heating resistor integrated with two types of sensors. The circuit as shown in figure 8(*a*) includes a series of five polysilicon stripes, each measuring $68\times11\,\mu$m, embedded in SiO_2 and protected by partially oxidized silicon nitride $Si_xO_yN_z$ and a relatively thick layer of polyamide. The resistors are used as heaters and have a total resistance of 460 Ω at room temperature. These resistors are integrated with a zigzag-shaped aluminium thermistor in a four-point configuration and two independent and equivalent sets of diode junctions. Details of calibration procedure for this device can be found in [43]. Figure 8(*b*) shows the thermal image of this integrated device obtained by thermoreflectance using a square modulation with $f = 7.5$ Hz and an illumination wavelength of 536 nm. The image results from an accumulation over 200 heating periods and a total acquisition time of 1 min with the spatial resolution of 360 nm. The average temperatures measured by thermoreflectance on the heater resistor and on the diode junction surface are obtained for various heating powers. The temperature increase, which is shown in figure 8(*c*), is in very good agreement with the temperatures measured by the four-point Al thermistor and the diodes and is also confirmed by simulation. All of these results have shown that the temperature changes linearly with the dissipated power as expected. Also, at the region where the diodes are implemented the temperature is almost 70% lower than the resistors' temperature. This suggests that the on-chip local temperature measurements by electrical sensors should be used with extreme care, since the junction sensors are usually in thermal contact with their substrate. In the case of the IC in this study, this effect has led to an underestimation of temperature of the metal strips [43].

5.4. Thermal mapping in optoelectronic devices

5.4.1. Edge-emitting laser diodes and quantum dot lasers. CCD-based thermoreflectance has been used to profile facet temperatures in edge-emitting laser diodes, where its ability to capture 2D images of temperature proves quite useful versus scanning point-based methods. In quantum dot lasers, it has been used to identify spatially separated heat sources within the device due to contact heating and non-radiative recombination, as well as to measure the thermal relaxation time constant of the active region itself [54].

5.4.2. High power laser diodes. As shown in figure 9, CCD-based thermoreflectance has been used to profile temperature in high-power lasers and quantify the effect of thermal lensing at high bias [55]. Thermoreflectance has furthermore been used to image the evolution of hot spots at laser facets, as shown in figure 10 [56].

5.4.3. Vertical cavity surface emitting lasers (VCSELs). Thermal effects are known to influence the performance of VCSELs through local gain compression, polarization switching, variations in the threshold current, decrease in the output power and self-focusing of the beam due to thermal lensing [57–61]. The most commonly used method of measuring temperature in VCSELs by monitoring the shift in lasing wavelength [59] provides only a spatially averaged temperature, which fails to resolve lateral and longitudinal temperature variations within the laser. Alternative methods include spatially resolved monitoring of the spontaneous electroluminescence wavelength shift (μ-EL) [62] and SThM [63]. μ-EL enables measurement of the radial temperature distribution of the top VCSEL mirror, with a demonstrated spatial resolution of 1–2 μm. SThM, which has been successfully demonstrated on a cross-sectioned VCSEL, is not suitable on a light emitting surface since the optical radiation is absorbed by the micro-thermocouple.

CCD-based thermoreflectance measurements have been reported on measuring the surface temperature of three types of 850 nm VCSELs (an oxide-confined single mode (SM)

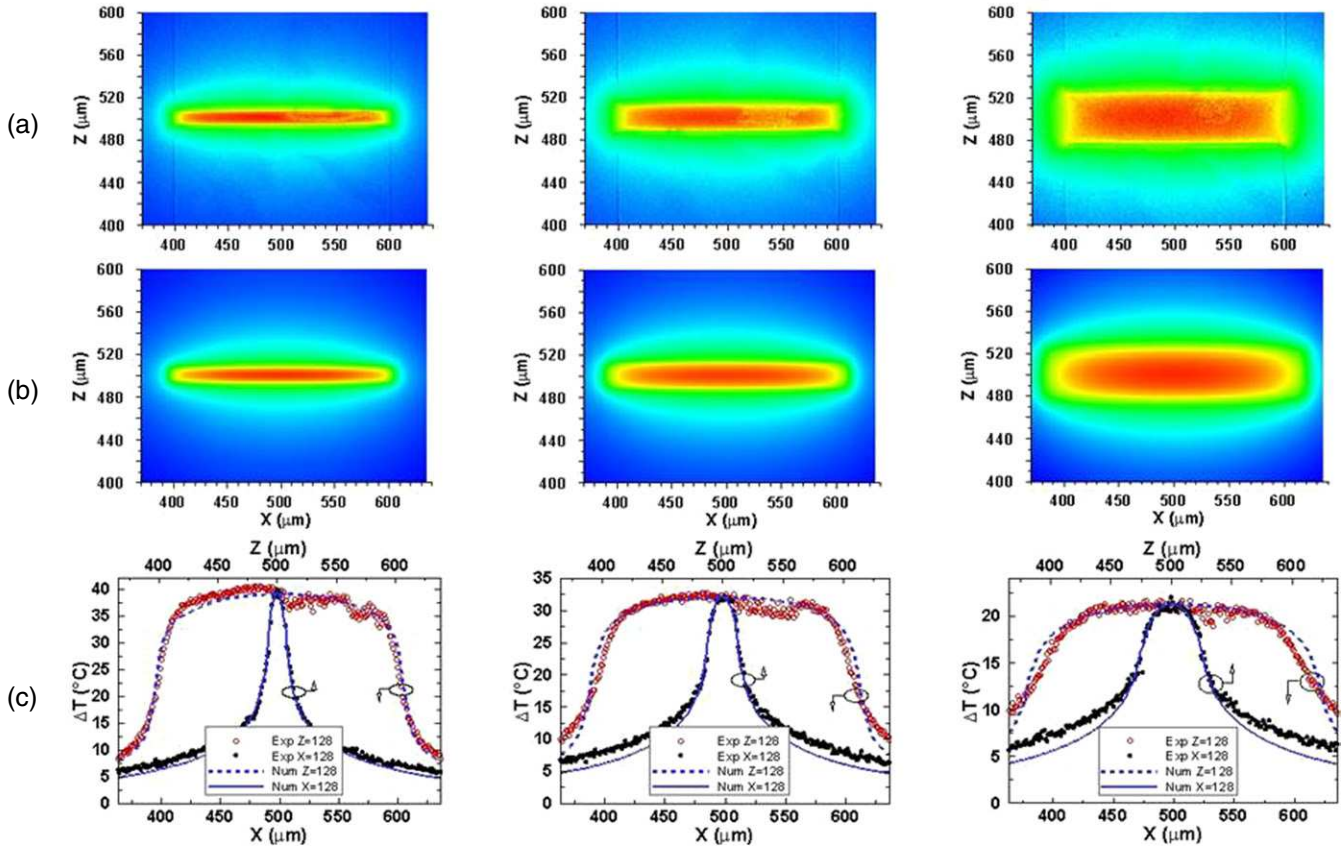

Figure 7. Comparison of experimental and numerical results for a micro-heater device at optimal parameters (*a*) measured temperature field on gold surface; (*b*) numerical solution over corresponding area; (*c*) line slices along mid-planes on the surface of the heater. From left to right: 14×200, 26×200 and $50 \times 200\,\mu$m. The thermal images in part (*a*) result from averaging over about 1000 heating cycles. (Reprinted with permission from [50]. Copyright 2007 IEEE.)

VCSEL, an oxide confined multimode (MM) VCSEL and a proton implanted MM VCSEL) under operating conditions [9]. Thermoreflectance images of an operating oxide-confined SM VCSEL, which show spatially resolved changes in surface temperature in response to a sinusoidal modulation of the injection current, are shown in figure 11. The VCSELs show higher temperatures near the central axis than at the edge. Taking the reported value for the thermoreflectance calibration coefficient κ into account, a temperature variation of about 40 °C between the centre and the edge of the VCSEL can be observed.

Combining the thermoreflectance images with a simple energy balance model [64] has shown that in all three types of VCSELs a linear relationship between the average surface temperature and dissipated power exists.

The measurements of the surface temperature distribution across the VCSEL aperture have also shown a convex thermal profile as a function of dissipated power. This picture is consistent with the thermal lensing phenomena in VCSELs which is more pronounced in SM VCSELs which are narrow-aperture devices.

5.4.4. Semiconductor optical amplifiers (SOAs) and photonic integrated circuits (PICs). Surface temperature measurements, in conjunction with an energy balance model, can be used to extract the optical power distribution and operating parameters of photonic devices. Demonstrated examples include stand-alone SOAs, diode lasers and SOA-based PICs, where spatially resolved thermoreflectance measurements have been used to determine the gain saturation length, to quantify optical gain and absorption parameters and to measure fibre coupling and splitter losses, among other operating parameters [65–67]. Furthermore, for SOA-based PICs, thermoreflectance imaging has been demonstrated to provide full characterization of the component photonic device parameters at the wafer scale, without the need for fibre coupling [68].

Figure 12 shows a schematic of a SOA-based Mach–Zehnder interferometer (MZI) with thermal images showing absorption and amplification of light in the input SOA under different operating conditions. When the SOA is unbiased, all optical power coupled from the input fibre is absorbed. This can be seen as an increase in the temperature at the input of the SOA (figure 12(*a*)) that decays exponentially with distance from the input in proportion to the power absorbed. Integrating under the absorption temperature profile allows the total coupled power to be calculated and, when compared with optical power measurements taken at the input fibre, can be used to determine fibre-to-chip coupling loss. In figure 12(*a*), for an input power of 40 mW measured at the fibre, an absorbed power of 14 mW in the SOA was measured using thermoreflectance, which gives a fibre-to-chip

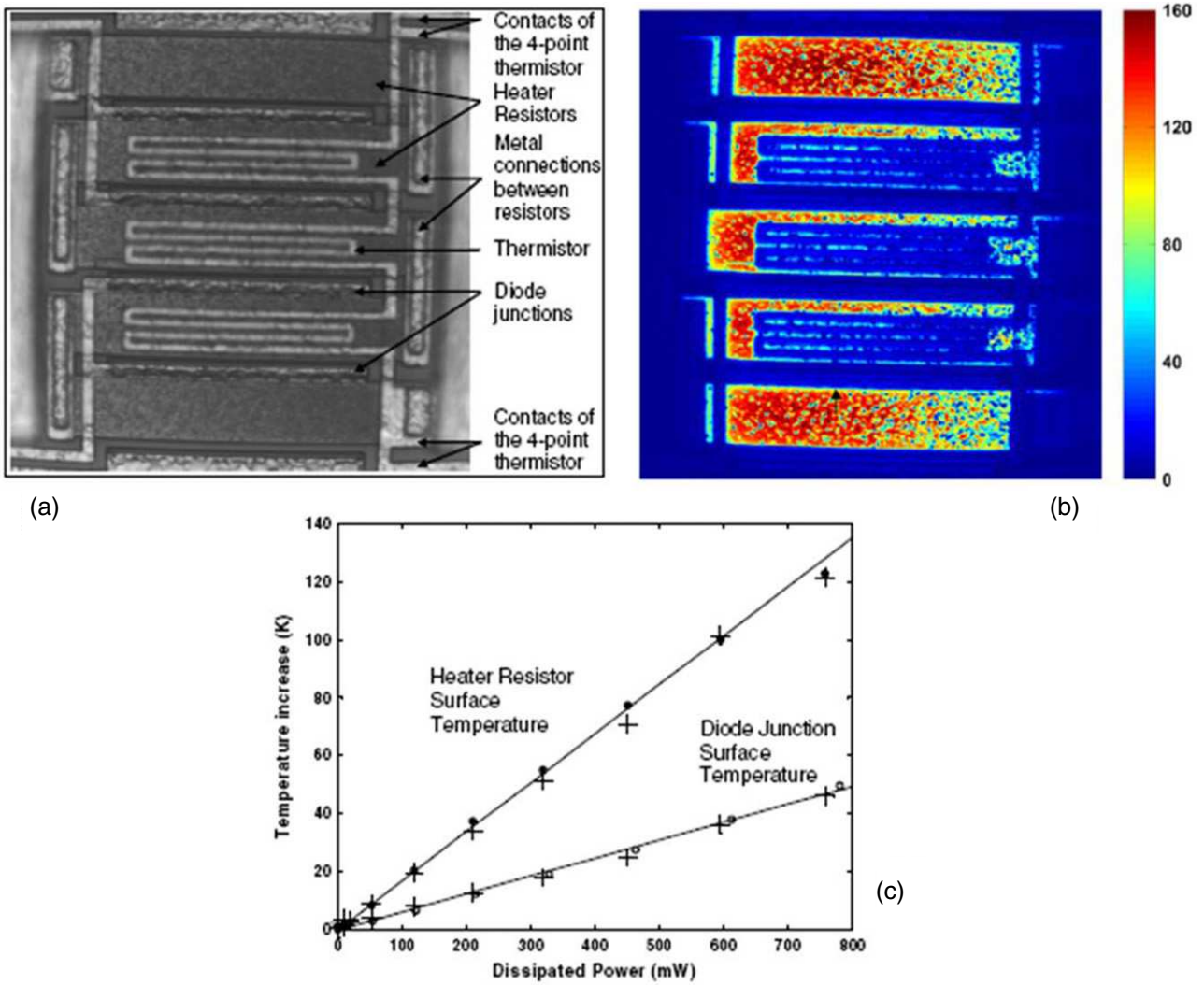

Figure 8. (*a*) Optical image of the polysilicon resistor stripes integrated with zigzag-shaped Al thermistors and two independent sets of diode junctions. (*b*) Thermal image obtained on the integrated resistors obtained with an illumination wavelength of 536 nm. The temperature scale bar gives the absolute temperature in the polysilicon only. (*c*) Average temperature measured by thermoreflectance (+) on the heater resistor and on the diode junction surface for various heating powers. Full dots show the temperature obtained by the four-point thermistor and open circles are the temperatures given by the diode. The lines are the results of simulation. (Reprinted with permission from [43]. Copyright 2006 IOP Publishing.)

coupling loss of 4.5 dB. These thermoreflectance power measurements are consistent with photocurrent measurements, but are advantageous in that they spatially resolve the SOA power distribution. This enables waveguide parameters to be extracted (e.g. an absorption coefficient, $\alpha \approx -4.8\,\mathrm{mm}^{-1}$ for the unbiased SOA in figure 12(*a*)) and can potentially be used for more precise design of SOA-based elements, such as saturable absorbers.

Figure 12(*b*) shows the thermal profile of the same SOA under normal operating conditions ($I = 300$ mA), where light coupled from the left SOA input is amplified as it propagates. Here, an increasing change in temperature can be seen towards the output of the SOA, as the light is amplified. Unlike the absorption measurements, the temperature profile seen during amplification corresponds to a decrease in temperature (i.e. optical cooling of the SOA), and is 180° out of phase with the absorption signal. Integrating the temperature profile along the length of the SOA allows measurement of the optical power added to the input signal, for calculation of the SOA gain and total output optical power. In figure 12(*b*), 3 mW of input optical power (measured at the fiber) is amplified to 14 mW at the SOA output, for an on-chip gain of nearly 11 dB. This ability to measure power at the output of the SOA is a unique attribute of thermoreflectance, and can be used with power measurements of devices down-chip to measure the loss of connecting components. For example, in the SOA-MZI schematic (figure 12(*c*)), the 14 mW output power measured from thermoreflectance in the input SOA can be used with photocurrent measurements in the top and bottom MZI SOAs to determine loss in the waveguide splitter and s-bends. Here, photocurrent measurements show 0.4 mW coupled into the bottom MZI SOA, for a total splitter and waveguide loss of 15 dB. Conventionally, this loss measurement would typically need to be made using special test structures or by modifying the PIC design to include power-monitoring electrodes. However, thermoreflectance obviates the need for such modifications, and measurements can be made non-invasively on an operating device.

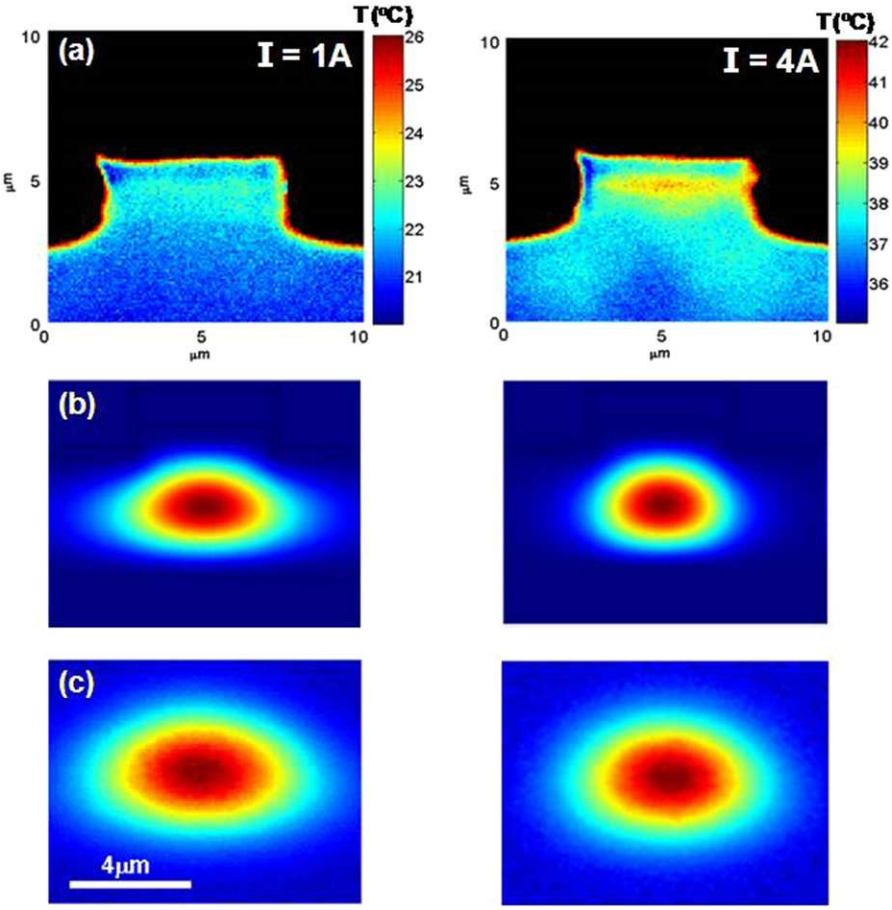

Figure 9. Measuring thermal lensing in high-power lasers. (*a*) Thermoreflectance images of high-power laser facet at two bias levels which resulted from about an hour total accumulation time. (*b*) Predicted optical modes based on the measured temperature profiles of part (*a*). (*c*) Direct measurements of optical modes confirming predicted thermal lensing [55].

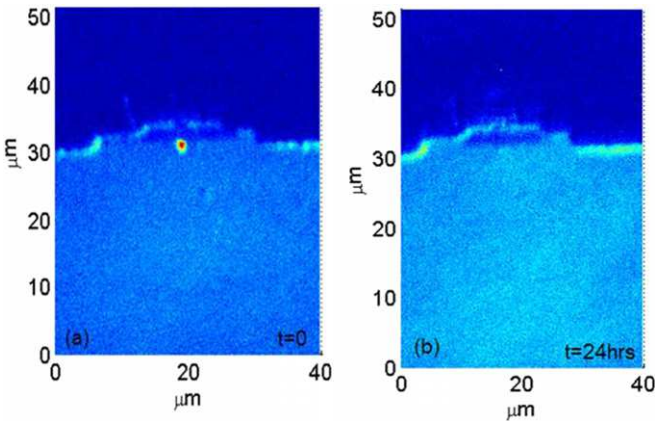

Figure 10. Laser facet hotspot imaged by CCD-based thermoreflectance. The hot spot appears in these $\Delta R/R$ images when the laser is first operated, but eventually disappears possibly due to localized facet damage [56]. The thermal images result from about an hour total accumulation time.

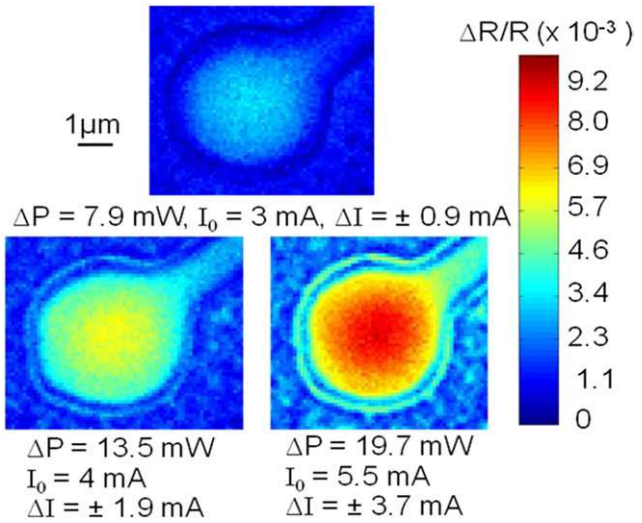

Figure 11. Typical thermoreflectance images of the oxide-confined SM VCSEL at three different dissipated power values. The images result from 6000 heating cycles at $f = 15$ Hz. (Reprinted with permission from [9]. Copyright 2007 IEEE.)

5.4.5. Electroabsorption modulators. Thermoreflectance images of an InGaAsP electroabsorption ridge modulator integrated with a tunable semiconductor laser operating at 1.55 μm are shown in figure 13 [69]. The thermal images were obtained using a P–I–N diode array camera with a 100 W mercury arc lamp. A thermoreflectance coefficient of $8.1 \times 10^{-5}\,\mathrm{K}^{-1}$ was obtained for the gold surface of the modulator using both thermocouple calibration and the method outlined by Dilhaire *et al* [70]. Figure 13(*b*) shows

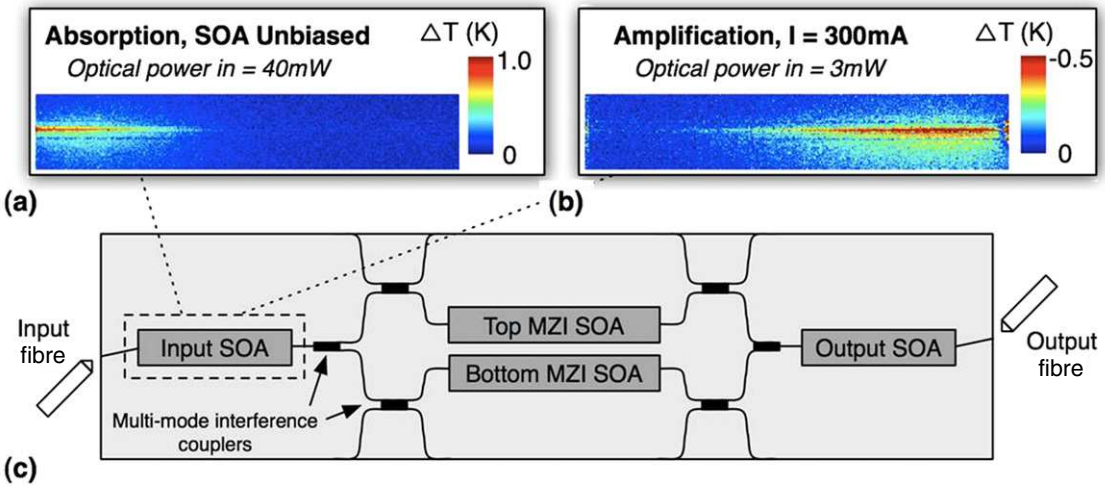

Figure 12. (*a*) Thermoreflectance image of heating in an unbiased SOA due to optical absorption. Change in temperature is proportional to absorbed optical power, which is largest at the SOA input (left side of image). (*b*) Thermoreflectance image of cooling in an SOA under normal biasing conditions. Cooling increases near the output of the SOA on the right, as the light is amplified. (*c*) Schematic of the SOA-MZI PIC from which the measurements were taken. The thermal images in parts (*a*) and (*b*) result from 5×10^5 heating cycles at $f = 15$ Hz, for a total accumulation time of 10 h.

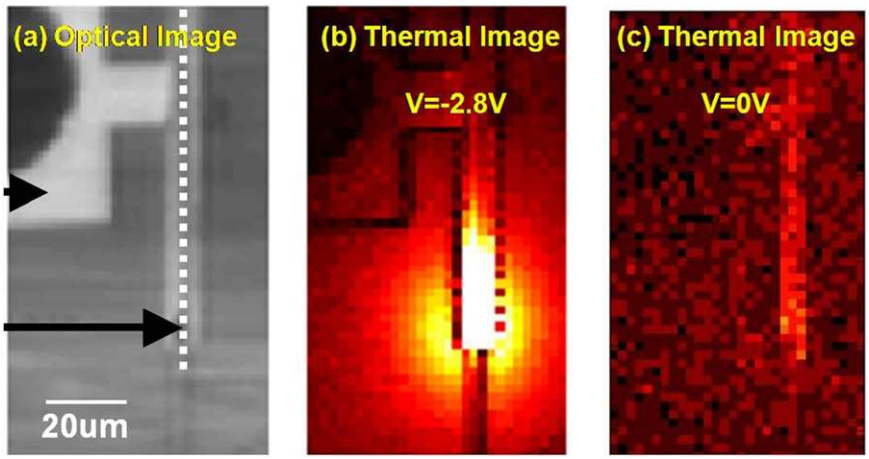

Figure 13. (*a*) Magnified image of an InGaAsP electroabsorption modulator. Thermoreflectance images showing heating in the modulator while in (*b*) the optically OFF state at −2.8 V and (*c*) the ON state at 0 V. Thermal images result from total accumulation time of about 2–3 min. (Reprinted with permission from [69]. Copyright 2003 American Institute of Physics.)

heating in the modulator during the optically OFF state at 2.8 V reverse bias. The temperature rise is due primarily to light absorption and heating at the input of the electroabsorption modulator. As the bandgap of the semiconductor shrinks at high temperatures, there is a positive feedback that increases the absorption coefficient and the localized heating at the input of the modulator. Temperature rise could reach 150 °C in the first 20 μm of the waveguide with optical power densities of ∼30 mW.

5.5. CCD-based TTR

5.5.1. Transient thermal imaging of thermionic micro-cooler. Critical thermal events in many micro-scale electronic and optoelectronic devices occur on the millisecond and microsecond time scale or faster. These fast transient thermal events are generally not observable when measuring steady-state heat response alone. Instead, fast transient thermal characterization techniques are required to measure rapid thermal mechanisms or to observe how device heating evolves in time. CCD thermoreflectance methods can be implemented to record 2D images of fast transient heating on a device surface with sub-microsecond time resolution [38]. The method maintains the advantages of good thermal resolution (50 mK) and sub-micrometre spatial resolution.

Figure 14 shows the fast TTR image sequence for a 20 × 20 μm SiGe thermionic micro-cooler which has a 2 μm gold top contact layer. The cooler is excited with a 700 mA pulse for 1 ms.

A thermoreflectance coefficient of $2.34 \times 10^{-4}\,^{\circ}\mathrm{C}^{-1}$ (at 540 nm illumination) was used to calibrate the temperature change on the top gold contact surface of the SiGe micro-cooler. This value was determined experimentally using the low-frequency micro-thermocouple calibration method described in section 4. Thermoreflectance profiles show the

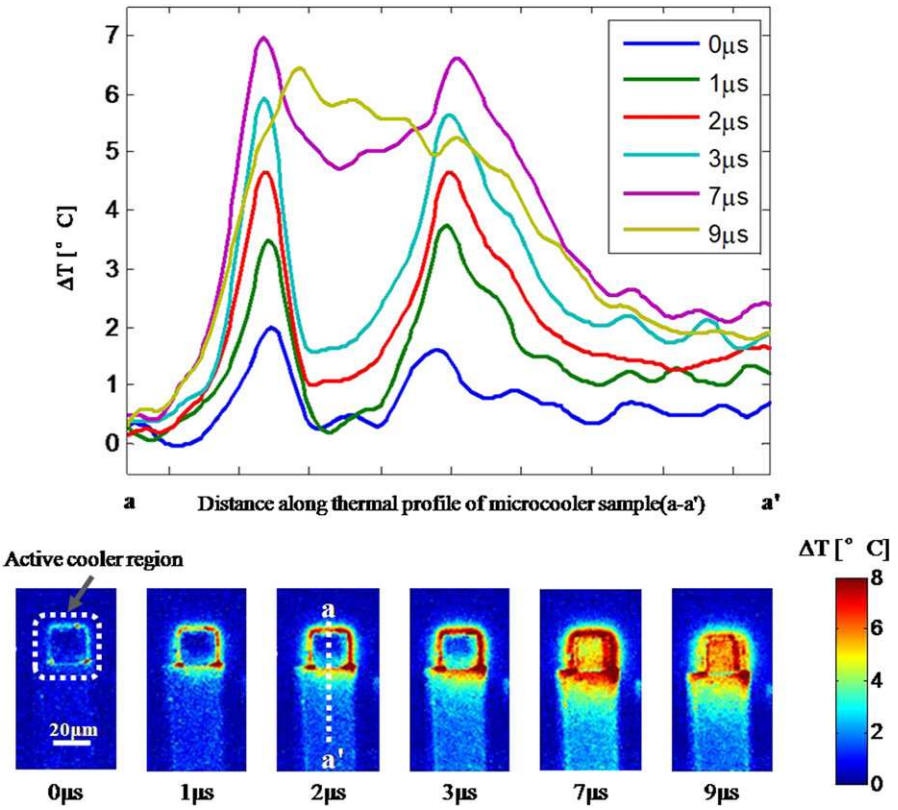

Figure 14. Fast TTR CCD images and profile for a 20 × 20 μm thermionic micro-cooler. Image sequence shows transient thermal response in the sample during the first 9 μs of device excitation with a 700 mA pulse. Thermal images result from averaging over about 12 000 heating cycles or about 8 min of total accumulation time.

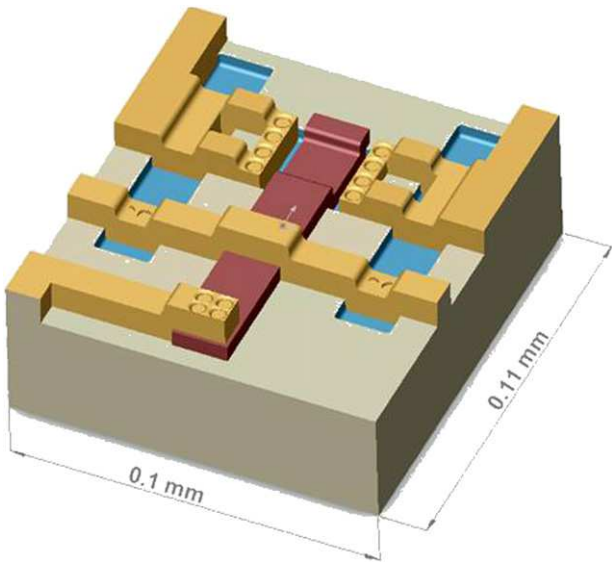

Figure 15. Geometry of the measured MOSFET device (field oxide omitted; vertical scale magnified by 20×). (Reprinted with permission from [37]. Copyright 2005 IEEE.)

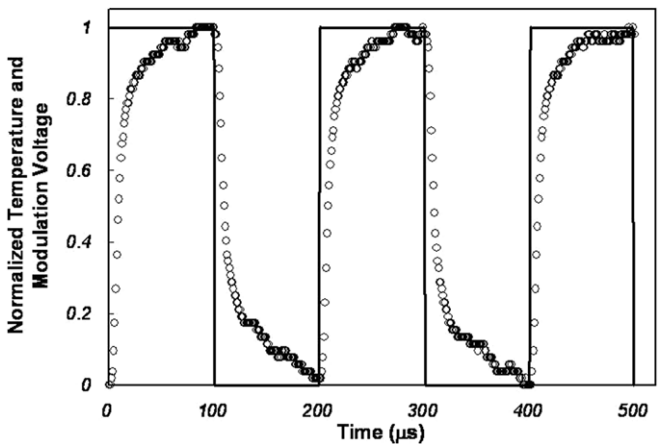

Figure 16. Transient normalized temperature and modulation signal (at hottest point on a MOSFET device). (Reprinted with permission from [37]. Copyright 2005 IEEE.)

temperature change along a cross-section of the sample surface including the substrate, active cooler region and contact lead. The sequence of thermal images records the time evolution of the temperature change in the device in the first 9 μs following the rising edge of the excitation pulse. Because the micro-cooler is biased in cooling mode, the active region remains cool during the first 3 μs. However, the amplitude of the current pulse is sufficient to introduce joule heating in the sample's lower layers at the device–substrate interface. This joule heating is slower, but eventually dominates the active cooling in the upper layers and at 7 μs into the transient thermal image sequence the effect of this heating becomes visible on the top surface. At 9 μs the device is effectively in thermal steady state. The fast transient thermal events occurring in the first few microseconds would not have been observed using steady-state

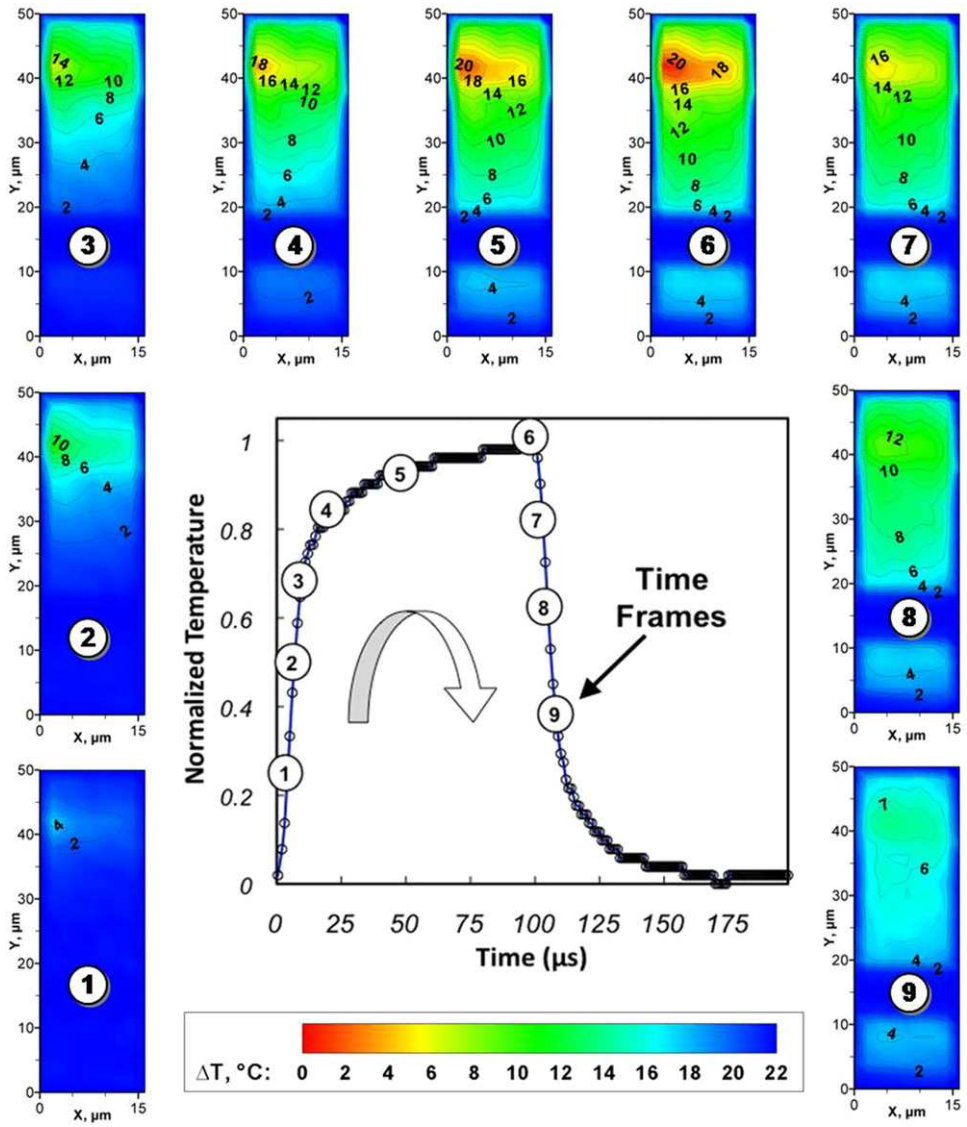

Figure 17. Temperature contours for the activated device during the heating phase of a pulse cycle. (Reprinted with permission from [35]. Copyright 2005 IEEE.)

thermal characterization. The images were obtained using the pulsed illumination boxcar averaging technique described in [38]. Time resolution of 800 ns was achieved by pulsing a 540 nm LED.

5.5.2. Laser-based TTR in MOSFET. The transient laser-based thermoreflectance temperature scanning measurements have been demonstrated on a typical MOSFET device. The geometry and structure of one of such devices is shown in figure 15. The oxide passivation layer, omitted in the schematic, is transparent to the probing laser used (488 nm), and hence does not figure in the optical measurements.

To increase the signal-to-noise ratio, the activation voltage of the device is modulated, resulting in a modulated photodetector signal that can more easily yield the useful signal from the raw photodetector signal. The outcome of each data collection after a pulsed activation is a transient waveform, an example of which is plotted with open symbols in figure 16, superimposed on the modulated activation voltage. After averaging over 256 waveforms, each containing 500 data samples, the transient reflectivity signature at a physical location is obtained with good accuracy (in the range of 1–2%). The temperature field over a region of interest can be mapped by repeating the above procedure at multiple physical locations [37].

To further demonstrate the capability of the system to provide transient surface temperature behaviour, snapshots of an animation of the temperature contours are shown in figure 17. The nine snapshots represent the surface temperature field at different instances in the heating and cooling phases of the full pulsed cycle. The time during the cycle of each of the contour plots is identified on the contour plot and on the waveform graph shown in the central part of figure 17. The snapshot times were chosen to graphically represent the transient thermal behaviour of the MOSFET device. This approach can provide an equally rich understanding of the

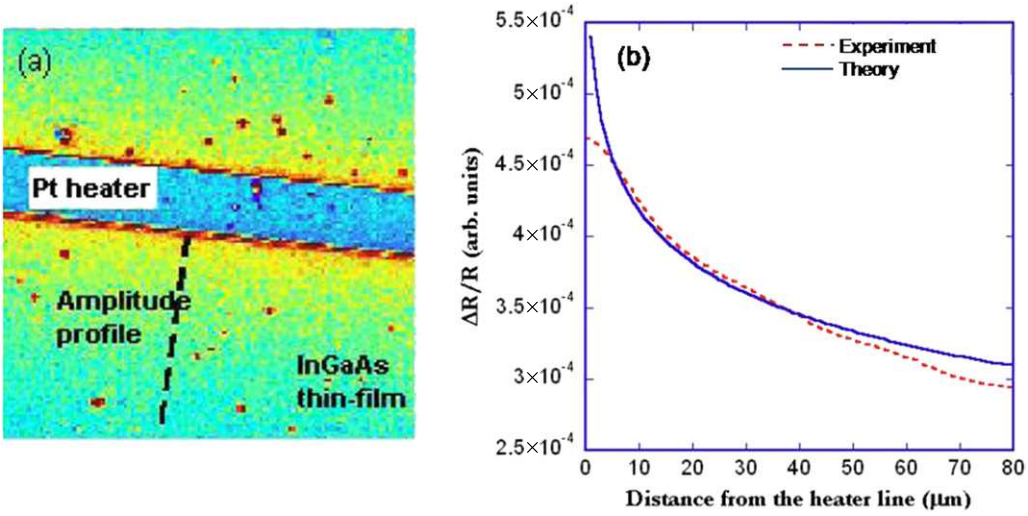

Figure 18. Determining thin film thermal conductivity using thermoreflectance imaging. (*a*) Thermoreflectance image showing the heat distribution from an active 30 μm wide metal heater line into an underlying InGaAs thin film. (*b*) Extracting thermal conductivity of thin film by fitting simulated thermal profile (perpendicular to heater axis) to thermoreflectance image data. Thermal images result from averaging over about 8000 heating cycles or about 40 min of total accumulation time. (Reprinted with permission from [73]. Copyright 2008 IEEE.)

transient thermal behaviour of devices that are operated at much higher pulse rates and/or at other duty cycles. Accounting for the uncertainties associated with the calibration and the actual temperature scanning, the overall random uncertainty of the results is estimated to be less than 13%.

5.6. Backside thermal imaging of ICs

Most of the heating in ICs occurs in the active layer below the surface. Near infrared (NIR) thermoreflectance microscopy has been demonstrated [71] to be able to provide thermal images of the buried layers inside the IC through the silicon substrate. The experimental setup for NIR thermoreflectance is similar to that with visible illumination light, except that for NIR measurement, an InGaAs CCD camera has been used. Under non-coherent illumination, thermal images with a diffraction-limited resolution of 1.7 μm have been obtained. Using a silicon solid immersion lens has further improved the resolution to 440 nm [71].

5.7. Thermal conductivity extraction in thin films

In addition to providing an effective complement to established temperature characterization techniques, thermoreflectance opens new approaches to existing characterization challenges. For example, the 3ω technique has become a standard electrical method for determining thermal conductivities of thin and bulk materials [72]. Thermoreflectance can be used to confirm 3ω electrical temperature measurements, but it can be employed as an independent, fully optical alternative method to determine thermal conductivity [73]. Figure 18(*a*) shows the thermoreflectance image of a 30 μm wide metal line heater deposited on top of an InGaAs thin film sample. In the 3ω technique, thermal conductivity of the underlying material (InGaAs) is obtained by measuring the temperature-dependent change in electrical resistance in the heater. However, thermal conductivity can also be determined by fitting experimentally obtained thermoreflectance profiles to simulations of the thermoreflectance amplitude as a function of perpendicular distance from the heater edge (figure 18). A distinct advantage of the optical approach is that any non-uniformity defects in the sample, such as localized heating due to current leaking into the thin film, would be instantly revealed by the 2D thermoreflectance temperature maps. Such a flaw would not be detected using purely electrical measurements. Another significant advantage of the optical detection is that it is not as sensitive if a very small fraction of current in the heater leaks to the substrate under study. A small leakage, which is common at high temperatures, can create slightly non-linear current–voltage characteristics which results in erroneous 3ω signal and in inaccurate thermal conductivity extraction.

6. Conclusion

In addition to the applications discussed in this review, as a thermography tool, CCD-based thermoreflectance microscopy technique has a great potential to be used by device manufacturers as a high-resolution non-invasive technique for quick failure analysis and temperature profiling of the devices under operating conditions. In some cases thermal images can serve as complementary information to the traditional electrical device test, and in other occasions they can detect flaws in the device that would not be detected even by these tests. The information provided by thermoreflectance, therefore, can be used for improvement of device and IC design. Other applications of CCD-thermoreflectance can also be implemented, such as thermal imaging of quantum cascaded lasers, solar cells and waveguides.

Acknowledgments

JAH would like to acknowledge the support of the National Science Foundation under Grant No ECS-0621735 and DMI-0531171.

KPP would like to acknowledge the support of the Defense Advanced Research Projects Agency through the EPIC programme under Grant NoW911NF-04-1-0429.

AS would like to acknowledge the support of National Semiconductor, UC Discovery programme as well as the Interconnect Focus Center funded by DARPA/SRC.

KM would like to thank James Christofferson of UC Santa Cruz for contributing thermoreflectance image data used in this paper.

References

[1] Raad P E, Komarov P L and Burzo M G 2008 Challenges in submicron thermal measurements and computations *1st Int. Symp. on Thermal Design and Thermophysical Property for Electronics (Tsukuba, Japan)*

[2] Brown J, Footner P K and Richards B P 1987 Failure analysis of plastic encapsulated components—the advantages of IR microscopy *J. Microsc.* **128** 179–94

[3] Christofferson J, Maize K, Ezzahri Y, Shabani J, Wang X and Shakouri A 2008 Microscale and nanoscale thermal characterization techniques *J. Electron. Packag.* **130** 041101

[4] Liu W and Yang B 2007 Thermography techniques for integrated circuits and semiconductor devices *Sensor Rev.* **27/4** 298–309 and the references therein

[5] Stephens C E and Suinnandurai F N 1974 A surface temperature limit detector using nematic liquid crystals with an application to microcircuits *J. Phys. E: Sci. Instrum.* **7** 641–3

[6] Kolodner P and Tyson J A 1982 Microscopic fluorescent imaging of surface temperature profiles with 0.01 °C resolution *Appl. Phys. Lett.* **40** 782–4

[7] Kolodner P, Katzir A and Hartsough N 1983 Remote thermal imaging with 0.7 mm spatial resolution using temperature dependent fluorescent thin films *Appl. Phys. Lett.* **42** 117–9

[8] Majumdar A, Lai J, Chandrachood M, Nakabeppu O, Wu Y and Shi Z 1995 Thermal imaging by atomic force microscopy using thermocouple cantilever probes *Rev. Sci. Instrum.* **66** 3584–92

[9] Farzaneh M, Amatya R, Lüerßen D, Greenberg K J, Rockwell W E and Hudgings J A 2007 Temperature profiling of VCSELs by thermoreflectance microscopy *IEEE Photon. Technol. Lett.* **19** 601–3

[10] Colclough A R 1992 *Temperature: Its Measurement and Control in Science and Industry* vol 6 (New York: American Institute of Physics)

[11] Vertikov A, Kuball M, Nurmikko A V and Maris H J 1996 Time-resolved pump-probe experiments with subwavelength lateral resolution *Appl. Phys. Lett.* **69** 2465–7

[12] Malyj M and Griffiths J E 1983 Stokes/anti-Stokes raman vibrational temperatures: reference materials, standard lamps, and spectrophotometric calibrations *Appl. Spectrosc.* **37** 315–33

[13] Matatagui E, Thompson A G and Cardona M 1968 Thermoreflectance in semiconductors *Phys. Rev.* **176** 950–60

[14] Guidotti D and van Driel H M 1985 Spatially resolved defect mapping in semiconductors using laser modulated thermoreflectance *Appl. Phys. Lett.* **47** 1336–8

[15] Christofferson J and Shakouri A 2005 Thermoreflectance based thermal microscope *Rev. Sci. Instrum.* **76** 24903

[16] Grauby S, Forget B C, Hole S and Fournier D 1999 High resolution photothermal imaging of high frequency phenomena using a visible charge coupled device camera associated with a multichannel lock-in scheme *Rev. Sci. Instrum.* **70** 3603–8

[17] Dilhaire S, Fournier D and Tessier G 2007 *Microscale and Nanoscale Heat Transfer* ed S Volz (Berlin: Springer) pp 239–86

[18] Clemens B M, Eesley G L and Paddock C A 1988 Time-resolved thermal transport in compositionally modulated metal films *Phys. Rev.* B **37** 1085–96

[19] Paddock C A and Eesley G L 1986 Transient thermoreflectance from thin metal films *J. Appl. Phys.* **60** 285

[20] Voigt P, Hartmann J and Reichling M 1996 Thermal wave imaging of electrically heated microstructures *J. Appl. Phys.* **80** 2013–8

[21] Mayer P M, Lüerßen D, Ram R J and Hudgings J 2006 Theoretical and experimental investigation of the resolution and dynamic range of CCD-based thermoreflectance imaging *J. Opt. Soc. Am.* A **25** 1156–63

[22] Filloy C, Tessier G, Hole S, Jerosolimski G and Fournier D 2003 The contribution of thermoreflectance to high resolution thermal mapping *Sensor Rev.* **23** 35–9

[23] Bellani V, Di Lernia S, Geddo M, Guizzetti G, Bosacchi A, Franchi S and Magnanini R 1997 Thermoreflectance study of the direct energy gap of GaSb *Solid State Commun.* **104** 81–4

[24] Ho C H, Li J H and Lin Y S 2006 Thermoreflectance characterization of interband transitions of $In_{0.34}Al_{0.66}As_{0.85}Sb_{0.15}$ epitaxy on InP *Appl. Phys. Lett.* **89** 191906

[25] Weakliem H A and Redfield D 1979 Temperature dependence of the optical properties of silicon *J. Appl. Phys.* **50** 1491–3

[26] Anderegg M, Feuerbacher B and Fitton B 1971 Thermoreflectance of graphite *Phys. Rev. Lett.* **26** 760–2

[27] Ozaki S and Adachi S 1995 Spectroscopic ellipsometry and thermoreflectance of GaAs *J. Appl. Phys.* **78** 3380–6

[28] Kwan C C Y and Woolley J C 1971 Electroreflectance and thermoreflectance of $ZnSiAs_2$ *Appl. Phys. Lett.* **18** 520–2

[29] Miyazaki T and Adachi S 1995 Analysis of spectroscopic-ellipsometry and thermoreflectance spectra of Si *J. Appl. Phys.* **77** 1741–6

[30] Baltz B 1972 *Semiconductors and Semimetals* ed R K Willardson and A C Beer vol 9 (New York: Academic) pp 315–402

[31] Seraphin O and Bottka N 1968 Band-structure analysis from electro-reflectance studies *Phys. Rev.* **145** 628–36

[32] de Freitas L R, da Silva E C, Mansanares A M, Tessier G and Fournier D 2005 Sensitivity enhancement in thermoreflectance microscopy of semiconductor devices using suitable probe wavelengths *J. Appl. Phys.* **98** 063508

[33] Mayer P M 2007 *PhD Thesis* Massachusetts Institute of Technology

[34] Grauby S, Salhi A, Rampnoux J-M, Michel H, Claeys W and Dilhaire S 2007 Laser scanning thermoreflectance imaging system using galvanometric mirrors for temperature measurements of microelectronic devices *Rev. Sci. Instrum.* **78** 074902

[35] Gammaitoni L, Hanggi P, Jung P and Marchesoni F 1998 Stochastic Resonance *Rev. Mod. Phys.* **70** 223–87

[36] Lüerßen D, Hudgings J A, Mayer P M and Ram R J 2005 Nanoscale thermo-reflectance microscopy with 10 mK temperature resolution using stochastic resonance *21st Annual IEEE SEMITHERM Symp. (San Jose, CA)* pp 253–8

[37] Burzo M G 2005 Noncontact transient temperature mapping of active electronic devices using the thermoreflectance method *IEEE Trans. Compon. Packag. Technol.* **28** 637–43

[38] Maize K, Christofferson J and Shakouri A 2008 Transient thermal imaging using thermoreflectance *24th IEEE SEMITHERM Symp. (San Jose, CA)* pp 55–8

[39] Tessier G, Hole D and Fournier D 2001 Quantitative thermal imaging by synchronous thermoreflectance with optimized illumination wavelength *Appl. Phys. Lett.* **78** 2267–9

[40] Tessier G, Jerosolimski G, Hole D, Fournier D and Filloy C 2003 Measuring and predicting the thermoreflectance sensitivity as a function of wavelength on encapsulated materials *Rev. Sci. Instrum.* **74** 495–9
[41] Amatya R and Hudgings J A unpublished
[42] Lüerßen D and Hudgings J A unpublished
[43] Tessier G, Polignano M L, Pavageau S, Filloy C, Fournier D, Cerutti F and Mica I 2006 Thermoreflectance temperature imaging of integrated circuits: calibration technique and quantitative comparison with integrated sensors and simulations *J. Phys. D: Appl. Phys.* **39** 4159–66
[44] Dilhaire S, Grauby S and Claeys W 2004 Calibration procedure for temperature measurements by thermoreflectance under high magnification conditions *Appl. Phys. Lett.* **84** 822–4
[45] Tessier G, Filloy C, Polignano M L, Mica I, Jerosolimski G, Hole D and Fournier D 2005 High resolution thermoreflectance imaging on transistor arrays with defect-induced leakage *J. Phys. IV France* **125** 423–5
[46] Komarov P L, Burzo M G and Raad P E 2006 CCD thermoreflectance thermography system: methodology and experimental validation *12th THERMINIC (Nice, France)*
[47] Grauby S, Dilhaire S, Jorez S and Claeys W 2005 Temperature variation mapping of a microelectromechanical systems by thermoreflectance imaging *IEEE Electron Dev. Lett.* **26** 78–80
[48] Chan P K L, Pipe K P, Qin G and Ma Z 2006 Thermoreflectance imaging of current dynamics in high power SiGe heterojuction bipolar transistors *Appl. Phys. Lett.* **89** 233521
[49] Raad P E and Komarov P L 2008 Thermal characterization of embedded electronic features by an integrated system of CCD thermography and self-adaptive numerical modeling *Microelectron. J.* **39** 1008–15
[50] Raad P E, Komarov P L and Burzo M G 2007 Non-contact surface temperature measurements coupled with ultrafast real-time computation *23rd IEEE SEMITHERM Symp. (San Jose, CA)*
[51] Raad P E, Komarov P L and Burzo M G 2007 An integrated experimental and computational system for the thermal characterization of complex three-dimensional submicron electronic devices *IEEE Trans. Compon. Packag. Technol.* **30** 597–603
[52] Wilson J S and Raad P E 2004 A transient self-adaptive technique for modeling thermal problems with large variations in physical scales *Int. J. Heat Mass Trans.* **47** 3707–20
[53] Burzo M G, Komarov P L and Raad P E 2002 A study of the effect of surface metallization on thermal conductivity measurements by the transient thermo-reflectance method *ASME J. Heat Trans.* **124** 1009–18
[54] Chan P K L, Pipe K P, Mi Z, Yang J, Bhattacharya P and Lüerßen D 2006 Thermal relaxation time and heat distribution in pulsed InGaAs quantum dot lasers *Appl. Phys. Lett.* **89** 011110
[55] Chan P K L, Pipe K P, Plant J J, Swint R B and Juodawlkis P W 2006 Temperature mapping and thermal lensing in large-mode, high-power laser diodes *Appl. Phys. Lett.* **89** 201110
[56] Chan P K L, Pipe K P, Mi Z, Yang J, Bhattacharya P and Lüerßen D unpublished
[57] Degen C, Fischer I and Elsasser W 2000 Thermally induced local gain suppression in vertical-cavity surface-emitting lasers *Appl. Phys. Lett.* **76** 3352–4
[58] Choquette K D, Richie D A and Leibenguth R E 1994 Temperature dependence of gain-guided vertical-cavity surface emitting laser polarization *Appl. Phys. Lett.* **64** 2062–4
[59] Lu B, Zhou P, Cheng J, Malloy K J and Zolper J C 1994 High temperature pulsed and continuous-wave operation and thermally stable threshold characteristics of vertical-cavity surface emitting lasers grown by metalorganic chemical vapor deposition *Appl. Phys. Lett.* **65** 1337–9
[60] Catchmark J M *et al* 1993 Extended temperature and wavelength performance of vertical cavity top surface emitting lasers *Appl. Phys. Lett.* **63** 3122–4
[61] Brunner M, Gulden K, Hovel R, Moser M and Ilegems M 2000 Thermal lensing effects in small oxide confined vertical-cavity surface-emitting lasers *Appl. Phys. Lett.* **76** 7–9
[62] Dabbicco M, Spagnolo V, Ferrara M and Scamarcio G 2003 Experimental determination of the temperature distribution in trench-confined oxide vertical-cavity surface-emitting lasers *IEEE J. Quantum Electron.* **39** 701–7
[63] Luo K, Herrick R W, Majumdar A and Petroff P 1997 Scanning thermal microscopy of a vertical-cavity surface-emitting laser *Appl. Phys. Lett.* **71** 1604–6
[64] Pipe K P and Ram R J 2003 Comprehensive heat exchange model for a semiconductor laser diode *IEEE Photon. Technol. Lett.* **15** 504–6
[65] Kapusta E W, Lüerßen D and Hudgings J A 2006 Quantifying optical feedback into semiconductor lasers via thermal profiling *IEEE Photon. Technol. Lett.* **18** 310–2
[66] Lüerßen D, Ram R J, Hohl-AbiChedid A, Clausen E Jr and Hudgings J A 2004 Thermal profiling: locating the onset of gain saturation in semiconductor optical amplifiers *IEEE Photon. Technol. Lett.* **16** 1625–7
[67] Hudgings J A, Pipe K P and Ram R J 2003 Thermal profiling for optical characterization of waveguide devices *Appl. Phys. Lett.* **83** 3882–4
[68] Farzaneh M, Ram R and Hudgings J A 2007 Fiber-free characterization of photonic integrated circuits by thermoreflectance microscopy *CLEO (Baltimore, MD)*
[69] Bian Z, Christofferson J, Shakouri A and Kozodoy P 2003 High power operation of electroabsorption modulators *Appl. Phys. Lett.* **83** 3605–7
[70] Dilhaire S, Jorez S, Patino Lopez L D, Batsale J C and Claeys W 2000 Calibration of temperature measurements upon micrometric metal lines applied to thermal conductivity identification of micrometric dielectric layers *Conf. on Heat Transfer and Transport Phenomena in Microsystems (Banff, Alberta, Canada)* p 392
[71] Tessier G, Bardoux M, Boue C, Filloy C and Fournier D 2007 Back side thermal imaging of integrated circuits at high spatial resolution *Appl. Phys. Lett.* **90** 171112
[72] Cahill D G 1990 Thermal conductivity measurement from 30 to 750 K: the 3ω method *Rev. Sci. Instrum.* **61** 802–8
[73] Maize K, Ezzahri Y, Wang X, Singer S, Majumdar A and Shakouri A 2008 Measurement of thin film isotropic and anisotropic thermal conductivity using 3ω and thermoreflectance imaging *24th IEEE SEMITHERM Symp. (San Jose, CA)*